

Aerodynamic Analysis of Morphing Nose Cone on Falcon 9

A PROJECT REPORT

Submitted by

**PRANCHAL GUPTA
(18103001)
BENNY MATHEW
(18103055)**

*in partial fulfilment for the award of the degree
of*

**BACHELOR OF TECHNOLOGY
in
AEROSPACE ENGINEERING**



**SCHOOL OF AERONAUTICAL SCIENCES
HINDUSTAN INSTITUTE OF TECHNOLOGY AND SCIENCE
PADUR, CHENNAI - 603 103**

MAY 2022

**HINDUSTAN INSTITUTE OF TECHNOLOGY AND
SCIENCE
PADUR, CHENNAI - 603 103**

BONAFIDE CERTIFICATE

Certified that this project report titled “**AERODYNAMIC ANALYSIS OF MORPHING NOSE CONE ON FALCON 9**” is the bonafide work of “**PRANCHAL GUPTA (18103001), BENNY MATHEW (18103055)**” who carried out the project work under my supervision. Certified further that to the best of my knowledge the work reported here does not form part of any other project/ research work on the basis of which a degree or award was conferred on an earlier occasion on this or any candidate.

HEAD OF THE DEPARTMENT

Dr. P. Vasanthakumar

Department of Aerospace Engineering

Hindustan Institute of Technology and
Science
Padur

SUPERIVIOR

Dr. M. Sai. Prakash

Associate Professor

Department of Aeronautical Engineering

Hindustan Institute of Technology and
Science
Padur

The Project Viva-Voce Examination is held on _____

Internal Examiner

External Examiner

ACKNOWLEDGEMENT

We would like to place on record our sincere thanks to all those who contributed to the successful completion of our final year project work.

It's a matter of pride and privilege for us to express our deep gratitude to the management of Hindustan Institute of Technology and Science for providing us with the necessary facilities and support.

We express our deep sense of gratitude to our respected Chairperson **Dr. (Mrs.) Elizabeth Verghese** and Pro-Chancellor **Dr. Anand Jacob Verghese** for giving us an opportunity to do the project.

We would like to thank our Director **Mr. Ashok Verghese** and Vice-Chancellor **Dr. S.N. Sridhara** for giving us moral support to complete this project.

We would like to express our grateful thanks to Dean (E&T)) **Dr. Angellina Geetha** and Registrar **Dr. Pon. Ramalingam** for support and encouragement.

We extend our sincere thanks to our Head of the Department **Dr. P. Vasanthakumar** for inspiring and motivating us to complete this project.

We would like to thank our guide **Dr M. Sai Prakash** for continually guiding and actively participating in our project, giving valuable suggestions to complete our project.

We would like to thank all the faculty members of the School of Aeronautical Sciences, who have directly or indirectly extended their support.

Last, but not least, we are deeply indebted to our parents who have been our greatest support while we worked day and night for the project to make it a success

LIST OF ABBREVIATIONS:

C_d = Drag Coefficient

CFD = Computational Fluid Dynamics

SMA = Shape Memory Alloys

AoA = Angle of Attack

L = overall length of the nose cone

R = ultimate radius

y = instantaneous changing diameter of the nose cone along x

x = distance from nosecone to tip

LIST OF FIGURES:

FIGURE NO.	TITLE	PAGE NO.
Figure 1.1	Wing Structure	1
Figure 1.2	Nose Cone of a rocket	2
Figure 1.3	Basic Principles of SMAs	3
Figure 2.1	Morphing Nose Cone Principle	5
Figure 2.2	Mechanism of Morphing Nose Cone	6
Figure 2.3	Design of Biomimetic Morphing Nose Cone	6
Figure 2.4	Fabricated model showing Contraction, Extension and Bending Motions	7
Figure 2.5	Various techniques used to study effects on increasing lift	7
Figure 2.6	Graph comparing C_d vs Mach Characteristics for various nose cone profiles	8
Figure 2.7	Comparing drag characteristics [(1)-Superior, (2)-Good, (3)-Fair, (4)-Inferior]	8
Figure 3.1	Nose Cone Geometry	9
Figure 3.2	Arc length for Parabolic nose cone	11
Figure 3.3	Arc length for Elliptical nose cone	11
Figure 4.1	Basic morphing nose cone	13
Figure 4.2	Velocity and Altitude Profile of the Rocket	13
Figure 4.3	Elliptical Nose Cone	15
Figure 4.4	$\frac{1}{2}$ Power Series Cone	16

Figure 4.5	Fixed Parameter Geometry	17
Figure 4.6	Phase 1	20
Figure 4.7	Phase 2	21
Figure 4.8	Phase 3	21
Figure 4.9	Phase 4	22
Figure 4.10	Phase 5	22
Figure 4.11	Phase 6	23
Figure 5.1	Computational Domain	25
Figure 5.2	Split Face Geometry For Meshing	26
Figure 5.3	Nose Cone Mesh	27
Figure 5.4	Mesh Granularity	27
Figure 5.5	Meshing at Nose Cone Apex	28
Figure 5.6	Boundary Layer at Nose Cone	28
Figure 5.7	Boundary Conditions-1	30
Figure 5.8	Boundary Conditions-2	30
Figure 5.9	Boundary Conditions-3	31
Figure 5.10	Fluent General Settings	32
Figure 5.11	Fluent Viscous Model	33
Figure 5.12	Fluent Material Properties	34
Figure 5.13	Fluent Material Properties Sutherland's Law	34
Figure 5.14	Fluent Cell Zone Conditions	35
Figure 5.15	Fluent Boundary Conditions	35
Figure 5.16	Fluent Boundary Conditions - Inlet	36
Figure 5.17	Fluent Boundary Conditions - Axis	36
Figure 5.18	Fluent Boundary Conditions - Body	37

Figure 5.19	Fluent Boundary Conditions - Nose Cone	38
Figure 5.20	Fluent Reference Values	39
Figure 5.21	Fluent Courant Number	39
Figure 5.22	Fluent Initialization	40
Figure 6.1	C_d vs Element Mesh Validation Graph	43
Figure 7.1	C_d vs Mach number for Ellipse	44
Figure 7.2	Drag force vs Mach number for Ellipse	45
Figure 7.3	C_d vs Mach number for Power series	45
Figure 7.4	Drag Force vs Mach Number for Power Series	46
Figure 7.5	C_d vs Mach number for Morphed Cone	47
Figure 7.6	Drag Force vs Mach number for Morphed Cone	47
Figure 7.7	Pressure contours at Mach 0.3 for Phase 1	48
Figure 7.8	Velocity contours at Mach 0.3 for Phase 1	48
Figure 7.9	Temperature contours at Mach 0.3 for Phase 1	49
Figure 7.10	Velocity contour at Mach 0.4 for Phase 2	49
Figure 7.11	Temperature contour at Mach 0.4 for Phase 2	50
Figure 7.12	Pressure contour at Mach 0.4 for Phase 2	50
Figure 7.13	Velocity contour at Mach 0.5 for Phase 3	51
Figure 7.14	Pressure contour at Mach 0.5 for Phase 3	51
Figure 7.15	Temperature contour at Mach 0.5 for Phase 3	52
Figure 7.16	Velocity contour at Mach 0.6 for Phase 4	52
Figure 7.17	Temperature contour at Mach 0.6 for Phase 4	53
Figure 7.18	Pressure contour at Mach 0.6 for Phase 4	53
Figure 7.19	Velocity contour at Mach 0.7 for Phase 5	54
Figure 7.20	Pressure contour at Mach 0.7 for Phase 5	54

Figure 7.21	Temperature contour at Mach 0.7 for Phase 5	55
Figure 7.22	Temperature contour at Mach 0.8 for Phase 6	55
Figure 7.23	Velocity contour at Mach 0.8 for Phase 6	56
Figure 7.24	Pressure contour at Mach 0.8 for Phase 6	56
Figure 7.25	Velocity contour at Mach 0.9 for Phase 6	57
Figure 7.26	Temperature contour at Mach 0.9 for Phase 6	57
Figure 7.27	Pressure contour at Mach 0.9 for Phase 6	58
Figure 7.28	Velocity contour at Mach 1 for Phase 6	58
Figure 7.29	Temperature contour at Mach 1 for Phase 6	59
Figure 7.30	Pressure contour at Mach 1 for Phase 6	59
Figure 7.31	Comparison of C_d vs Mach Characteristics for Morphed Nose cone, Elliptical Nose cone, and $\frac{1}{2}$ Power series	61
Figure 8.1	Example for Morphing Supersonic Nose Cone	62
Figure 8.2	Change in Angle of Attack using Morph Nose cone	63

LIST OF TABLES:

TABLE NO.	TITLE	PAGE NO.
Table 3.1	Each nose cone shape has a radius that corresponds to an incremental step in length along the nose cone. The difference in radius between the two nose cone designs is seen in the right column	12
Table 4.1	Atmospheric Conditions	14
Table 4.2	Initial Nose Cone Parameters	15
Table 4.3	Fixed Parameters	17
Table 4.4	Change in radius of the ribs	19
Table 4.5	Change in length of nose cone for different phases	20
Table 5.1	Boundary Conditions	31
Table 6.1	y^+ Plot	41
Table 6.2	C_d readings at different element quantity	42
Table 7.1	C_d values for ellipse, power series and morphed nose cone for comparison	60

ABSTRACT:

This project aims to analyze the aerodynamic characteristics of a morphing nose cone, specifically the C_d vs Mach No characteristics. Two nose cone profiles have been selected (ellipse, $\frac{1}{2}$ power series). A hypothetical mechanism was designed to study the morphing of the nose cone. The mechanism is designed in such a way that the nose cone's arc length remains constant, while the nose length increases, and the ribs' lengths decrease linearly with time. In the mechanism, aerodynamic heating is also considered, and a titanium tip could be used, as the aerodynamic heating is very high at the nose tip. The nose cones are attached to a representation of the Falcon 9 rocket, and simulations are run for different Mach Numbers (from 0.3 to 1), results are calibrated for morphed nose cones through phase transformation. The C_d vs Mach No. characteristics are plotted for the both, then the nose cone is morphed from Mach 0.3 to Mach 0.8, and their combined C_d vs Mach No. graphs are plotted. The three graphs are compared to confirm whether the morphed nose cone gives better drag characteristics than either of its static parent nose cones.

TABLE OF CONTENTS:

CHAPTER NO.	TITLE	PAGE NO.
	List of Abbreviations	iv
	List of Figures	v
	List of Tables	ix
	Abstract	x
1	INTRODUCTION	1
2	LITERATURE REVIEW	5
3	METHODOLOGY	9
4	DESIGN	
	4.1 Initial Assumptions and Conditions	13
	4.2 Parameters	14
	4.3 Nose Cone Geometry	15
5	SETUP	
	5.1 Computational Domain	24
	5.2 Meshing	25
	5.3 Fluent Settings	28
	5.4 Boundary Conditions:	31
	5.5 Fluent Setup	32

6	VALIDATION 6.1 Y+ Values 6.2 Mesh Independence Study	41 42
7	ANALYSIS	44
8	FUTURE ENHANCEMENT AND CONCLUSION 8.1 Conclusion	62 64
9	REFERENCES	65

1. INTRODUCTION

The aerospace industry has been researching techniques to improve aerodynamic performance and maximize lift-to-drag ratio in all flying circumstances. Currently, fixed wings are used extensively all over the world. but the outcomes are not what researchers and designers had hoped for. To address this, researchers looked all the way back to when the Wright Flyer used twist morphing and came up with a way to use and improve morphing wing technology. The morphing wing is the best approach to obtain high aerodynamic performance and also improve lift to drag ratio in all flight scenarios by altering its shape depending on the situation, where the fixed wing cannot be used properly and efficiently in all flight conditions.

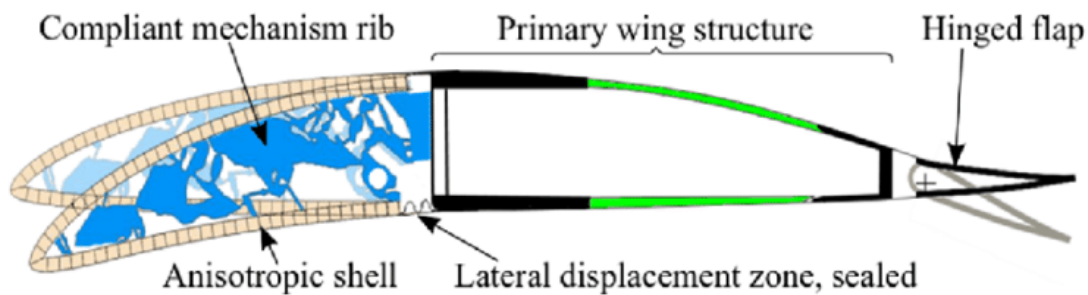


Figure 1.1: Wing Structure

The nose cone of a spacecraft or rocket has to be taken into account as it significantly affects the drag on the body of the vehicle, generally through its shape. Furthermore, for reentry vehicles and tactical missiles, the temperature of the nose cone induced by aerodynamic heating ranges from 2000 to 3000 degrees Celsius. As a result, among a variety of design requirements, the major issue in the design of these supersonic and hypersonic vehicles is the decrease of both drag and aerodynamic heating. Thus, in the design of the nose cone, shape optimization is crucial. Numerous studies have been conducted on the design and optimization of the nose cone form.



Fig 1.2: Nose Cone of a rocket

At different Mach ranges, different nose cone shapes have the optimal drag characteristics. Since a vehicle has only one nose cone, this means that no matter which nose cone is chosen for the vehicle, there is always a performance tradeoff since the nose cone with the best drag characteristic at one velocity is sub-par at another.

Morphing technology has been gaining significant interest over the last three decades since it could enhance the performance and efficiency of a craft over a wide range of flight conditions. The Aircraft Morphing Program was established by NASA in order to develop and mature smart component technologies for advanced airframe systems that may be incorporated in aircraft structures and deliver cost-effective system benefits.

The use of a shape memory alloy was suggested to accomplish this mid-flight change in nose cones. The term "smart materials," sometimes known as "intelligent materials," refers to a set of material molecules that have distinct features. When the smart material is exposed to electrical, thermal, or magnetic forces, these unique features are frequently related to a significant strain deformation.

Piezoelectric or electrostrictive materials are smart materials that distort when exposed to an electric field. Piezoelectric materials can deform in both compression and

elongation, whereas electrostrictive materials typically deform in one of two ways: elongation or compression. Shape Memory Alloys are smart materials that respond to a thermal field (SMA). Large deformations and phase transitions are visible in these materials. However, as compared to piezoelectric materials, their response is extremely slow.

The Phase Transformation Process for SMAs

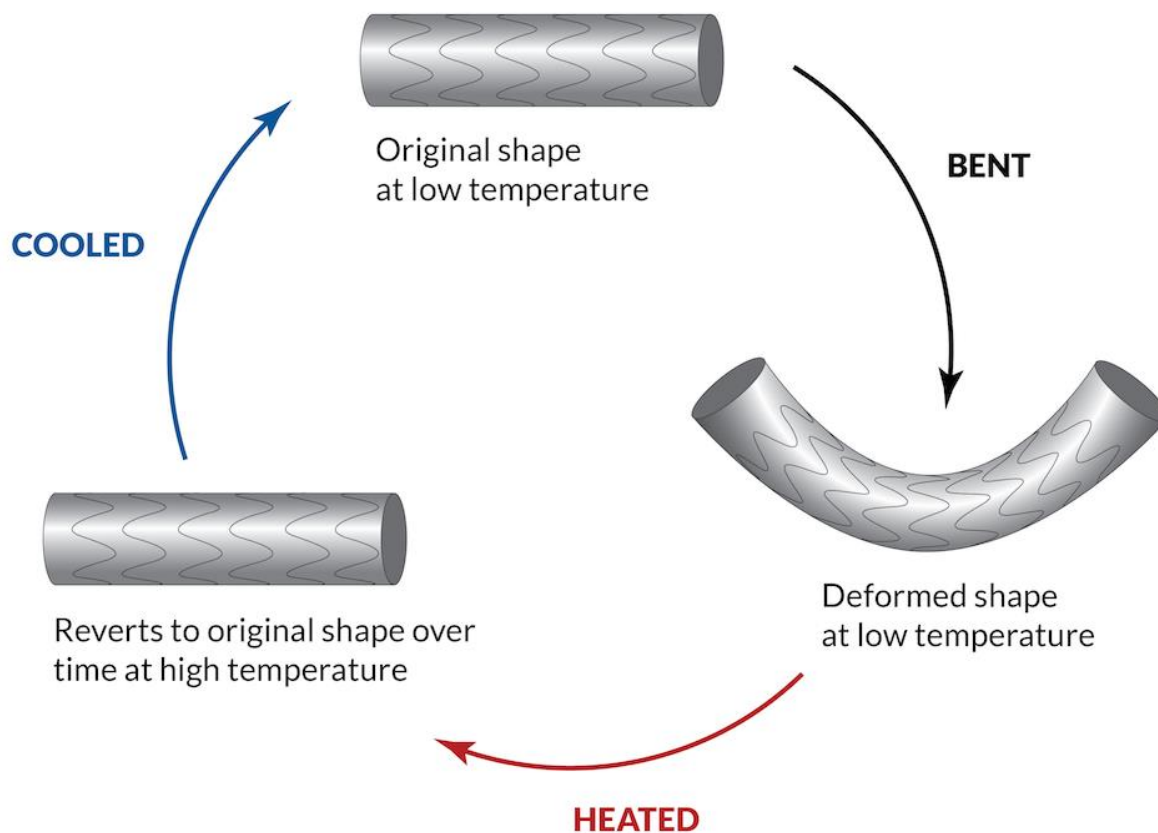


Fig 1.3: Basic Principles of SMAs

Magnetostrictive materials are smart materials that respond to magnetic fields. Magnetostrictive materials, like electrostrictive materials, can exhibit anisotropic behavior. Shape memory alloys that respond to magnetic fields are also available. Ferromagnetic Shape Memory Alloys are the name given to these alloys (FSMA)

Unfortunately, few studies have been conducted so far on the topic of morphing nose cones, but it is likely that this field will garner greater attention over time as researchers seek to improve the drag efficiency of the spacecraft, and look beyond the morphing of wings to attain the desired results.

2. LITERATURE REVIEW

Li *et al* (2013) proposed a conceptual design for morphing nose cones, with deformable shapes at different flight phases. The structure of a morphing nose cone is conceptually designed. To determine the ideal geometric parameters of the morphing structure, a genetic algorithm is used to construct a mechanical design and optimization approach. The proposed method is applied to an example. The results demonstrate that the best option provides the least amount of position inaccuracy. The morphing nose cone design gives an innovative approach to reduce reentry vehicle drag. The proposed method could be utilized to build and optimize the deployable structure of morphing nose cones in the real world. It is blunt upon exiting the atmosphere, shifting to a sharper cone upon reentry to reduce drag. It uses a mechanism consisting of several slider-crank units, each of which has two links and a slider.

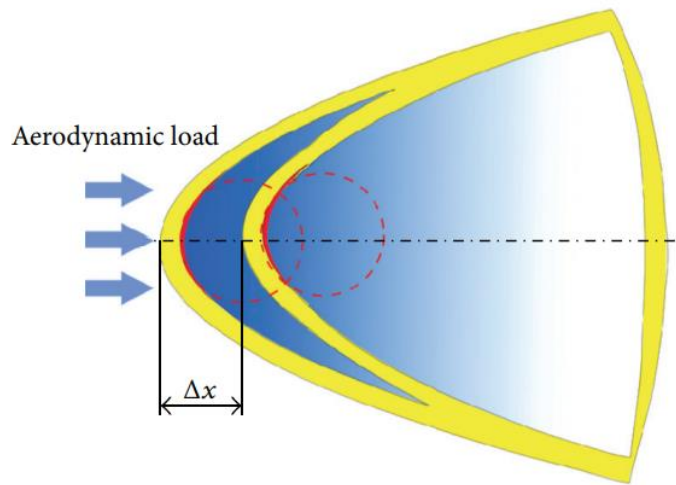


Fig 2.1 : Morphing Nose Cone Principle

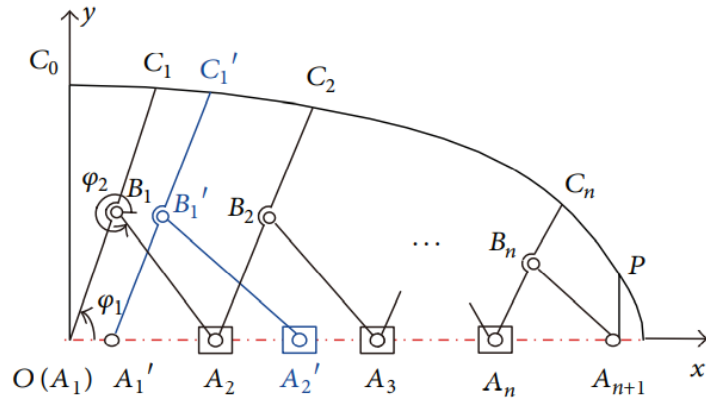


Fig 2.2: Mechanism of Morphing Nose Cone

Zhao *et al* (2019) proposed a conceptual nose cone design that was inspired by the abdomen of a honeybee, including its ability to manipulate its shape as desired. In this study, a biomimetic skeleton structure of a morphing nose cone is created, which can stretch and flex continuously and is inspired by the changeable geometry mechanism of honeybee abdomen. The degree of freedom of a morphing nose cone is computed using the screw theory. Then, for the morphing nose cone, a prototype of a biomimetic skeletal structure with six parts was created. The deformation ability and dynamic performance of the morphing nose cone are further evaluated through simulation analysis and experimental testing. The results reveal that the morphing nose cone's deformation ability satisfies the design requirements. The morphing nose cone's driving mechanism's flexibility creates high-frequency components, which significantly lowers its dynamic performance.

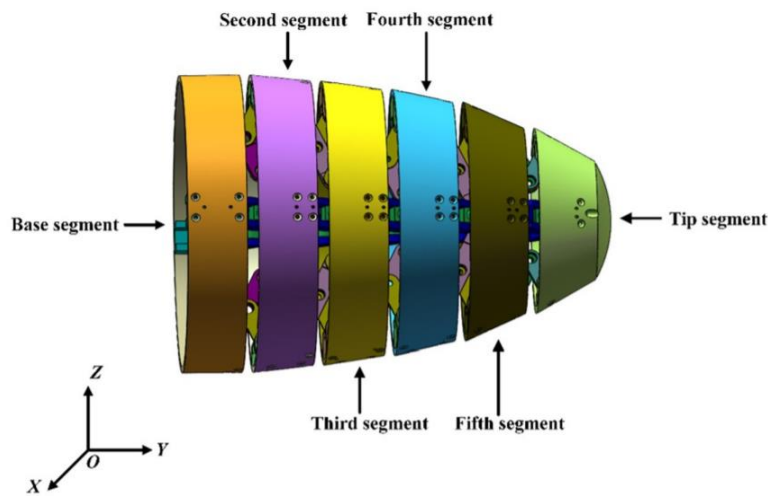


Fig 2.3: Design of Biomimetic Morphing Nose Cone

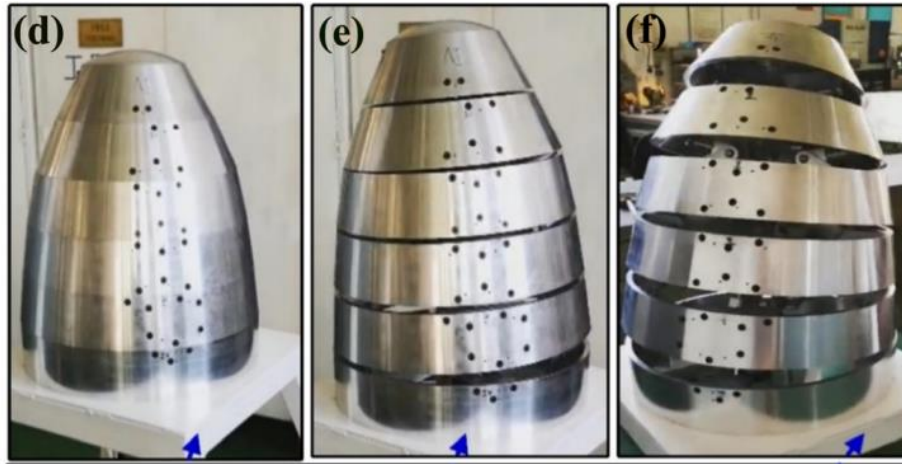


Fig 2.4: Fabricated model showing Contraction, Extension and Bending Motions

Stephen *et al* (2019) investigated the usefulness of modifying the nose cone of a subsonic missile (at $M = 0.3$) in enhancing the characteristics of the nose cone for flight control over subsonic conditions. Three techniques were studied to flatten the nose cone, granting a larger lifting area. There were three different approaches taken. The conventional method of integrating aerodynamic surfaces (strakes) to the articulating portion of the nose was an option. Two distinct sizes were used. The second method is to create a morphing nose that can flatten to create a greater lifting surface, and the third method is to reconfigure the nose to the form of a bird of prey's head. The strakes were effective, resulting in a 500% increase in the missile's trimmed lift. The strakes also generated a large amount of drag to the vehicle.

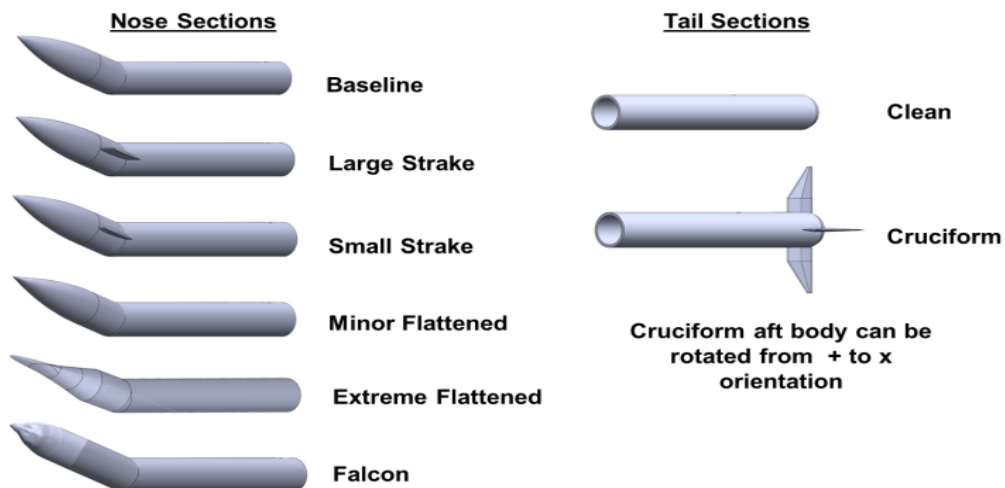


Fig 2.5: Various techniques used to study effects on increasing lift

Iyer *et al* (2020) examined various nose cone designs, primarily for high performance vehicles, and the factors to be considered for aerodynamic optimization. In subsonic flow regimes, an elliptic nose cone is favored, whereas Von Karman is favored for slightly above subsonic to transonic flow regimes. In supersonic flow, design is mainly about balancing different types of drags. However, in hypersonic flow, aerodynamic heating is a major concern, and the nose cone's geometric characteristics must be chosen accordingly.

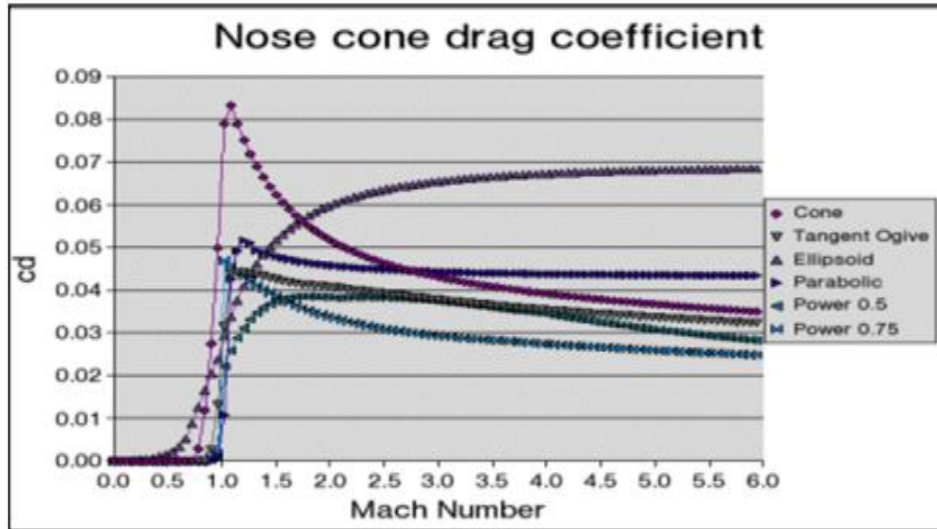


Fig 2.6: Graph comparing C_d vs Mach Characteristics for various nose cone profiles

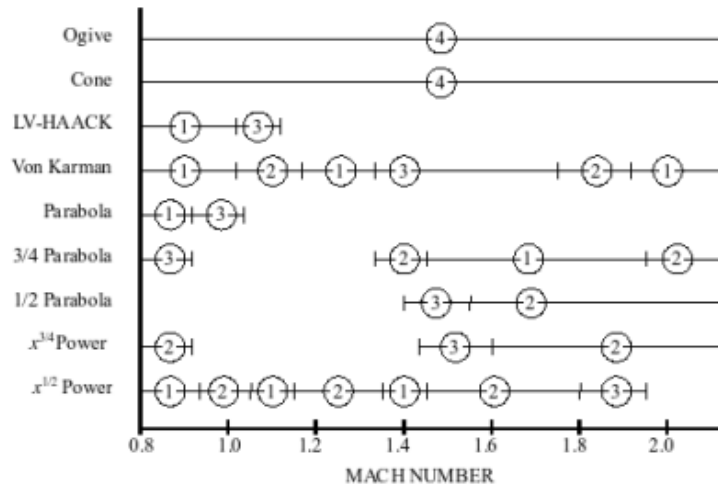


Fig 2.7: Comparing drag characteristics [(1)-Superior, (2)-Good, (3)-Fair, (4)-Inferior]

3. METHODOLOGY

This project takes the most basic principle of morphing nose cones : the nose cone changes shape by increasing or decreasing the width while decreasing or increasing the nose length respectively.

A hypothetical model having its ribs made of SMAs that reduce in width is taken and studied.

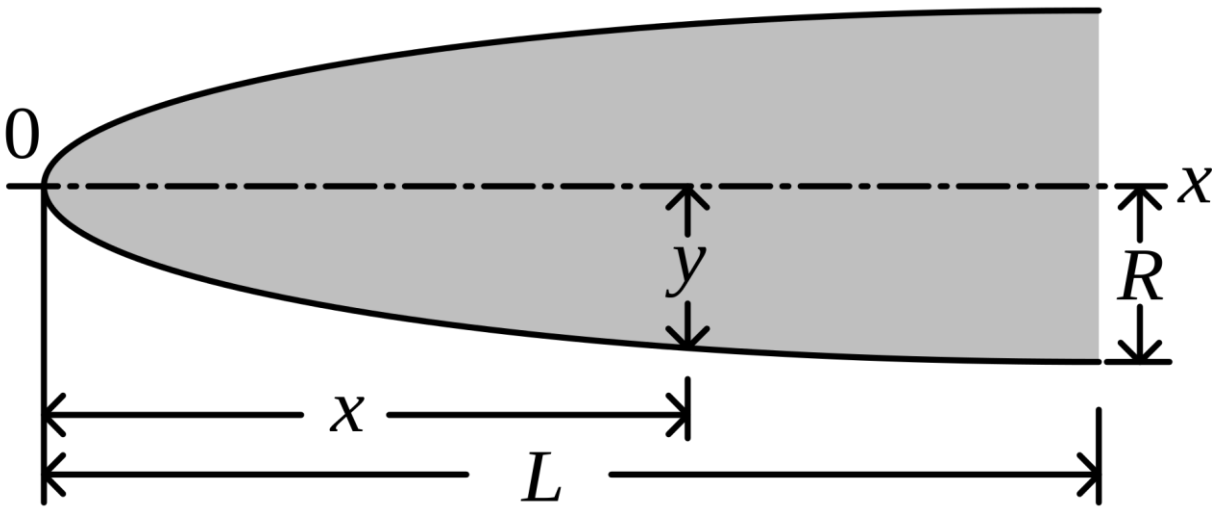


Fig 3.1: Nose Cone Geometry

where L is the overall length of the nose cone, R is the ultimate radius, and y is the instantaneous changing diameter of the nose cone along x, the increasing distance from nosecone follow to tip,

The governing equations for the curvature of each nose cone shape are as follows:

Elliptical

$$y = R \sqrt{1 - \frac{x^2}{L^2}}$$

1/2 Power Series

$$y = R * \left(\frac{x}{L}\right)^{0.5}$$

Creo parametric software was used to create the nose cone for the Falcon 9. The first step is to develop a 2D model for CFD testing using the equations described above.

CFD analysis is performed in three steps:

- (i) preprocessing, geometry – designing, meshing, boundary conditions, and numerical method;
- (ii) processing – solving fluid flow governing equations numerically until convergence is achieved; and
- (iii) post processing – extracting results in terms of graphs, contours, and required results.

The above three phases are carried out in ANSYS using fluid fluency CFD for design and meshing with an Inflation Layer around the nose to capture the boundary layer and a structured grid with tetrahedral cells containing roughly 0.6 million elements. Simulations are performed using the ANSYS CFX finite volume solver with inlet parameters of Mach 0.2, 0.3, 0.4, 0.5, 0.6, 0.7, 0.8, 0.9, 1.0 for each nose using the fluid fluent model.

Step changes in radius for each nosecone form were investigated in order to build the outside shell of the nosecone with the potential to endure shape modifications from the Elliptical to the $\frac{1}{2}$ Power Series nose cone keeping the Arc length (Nose Curve Surface Length) the same at all phases. Starting at the tip of the nose cone geometry, incremental magnitude changes were used to construct the corresponding radius of the nose cone morphologies at each of these lengths. Table 1 is an example of this information. The distance the nose cone had to shift to transition from Elliptical to a $\frac{1}{2}$ Power Series shape was determined by the difference in radii.

Arc Length = 539.712 inches (13.7086 m) : Constant

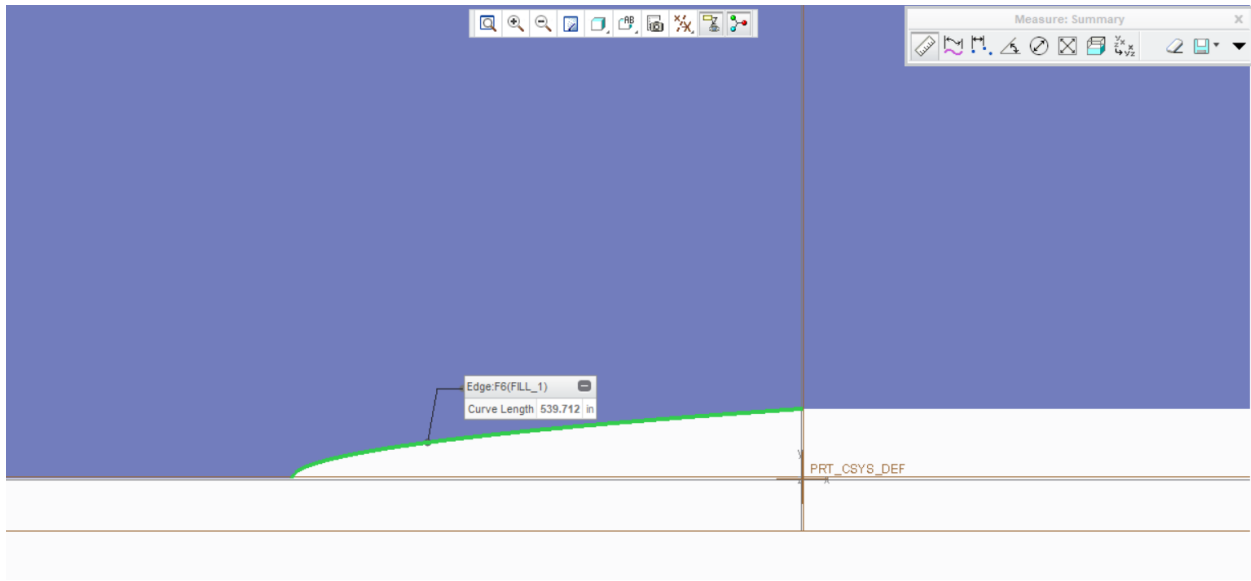


Fig 3.2: Arc length for Parabolic nose cone

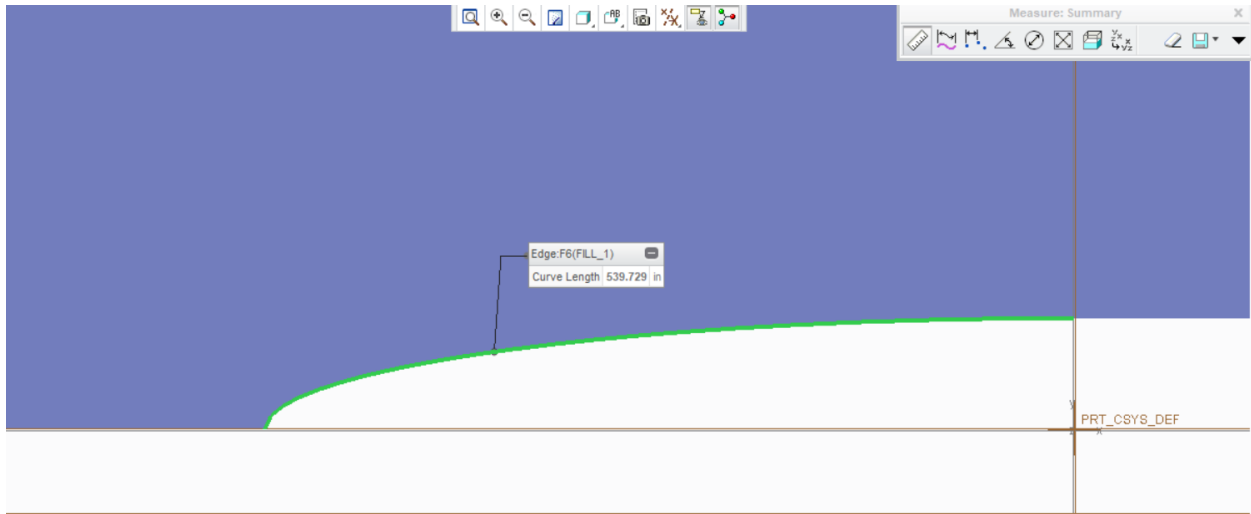


Fig 3.3: Arc length for Elliptical nose cone

Table 3.1 : Each nose cone shape has a radius that corresponds to an incremental step in length along the nose cone. The difference in radius between the two nose cone designs is seen in the right column

Nose Length X (inc)	Elliptical Nose Y _{EN} (inc)	½ Power Nose Y _{PN} (inc)	Difference
0	72	72	0
40	71.79119448	69.2318552	2.559339287
90	70.93660199	65.60763668	5.328965304
140	69.39885563	61.77114381	7.627711821
190	67.13102555	57.68003489	9.45099066
240	64.05561479	53.27568528	10.77992951
290	60.04866982	48.47278473	11.57588509
340	54.90662505	43.13841765	11.7682074
390	48.26806364	37.04369439	11.22436925
440	39.38334961	29.7245271	9.658822512
490	26.04734636	19.87107769	6.176268668
520	10.48223618	10.08201661	0.4002195728
525.6	0	6.849381516	-
530.4	-	0	-

4. DESIGN:

4.1 Initial Assumptions and Conditions

The nose cone is being tweaked to fit a certain velocity profile. The velocity and altitude profile of the Falcon 9 rocket are depicted in the image below. The rocket's nose cone, as depicted here, will reach Mach 3 speeds. The chosen velocity range is subsonic (Mach 0.2-1).



Fig 4.1: Basic morphing nose cone

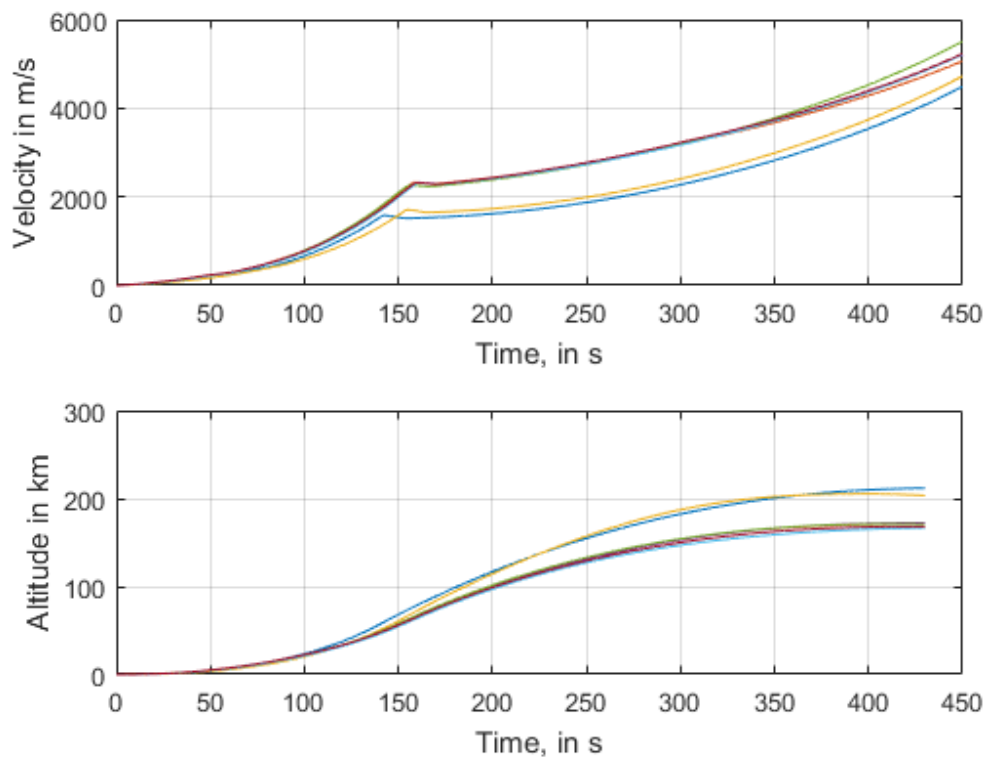


Figure 4.2: Velocity and Altitude Profile of the Rocket.

While the rocket is predicted to reach a height of 200 kilometers and experience a variety of variations in pressure, temperature, and other variables, a few assumptions

were made to make the simulations easier. The initial assumption is that the nose cone simulations will be conducted in a wind tunnel at sea level, as shown in table 1. Second, no changes in free-stream temperature, pressure, or any other factors are assumed. Simulators for all nose cone geometries will be run in the same way and in the same environment. Third, with the oncoming wind, it is anticipated that the nose cone will be at zero AOA.

Table 4.1: Atmospheric Conditions

Parameter	Value
Pressure	101.325 kPa
Temperature	300 K
Density	1.18 kg/m ³
Viscosity	8.90 × 10 ⁻⁴ Pa·s

4.2 Parameters

Based on the information collected from both the reference material and studies the nose cone geometry selected was from the Elliptical to the ½ Power Series nose cone . As stated in the conditions above, the outside diameter of the nose cone geometry is fixed. The only variables that varied were the ribs diameter and length. The starting parameters of the design and their values are provided in the table 2 below. These parameters were based on previous year’s design and served as the initial values for the optimization process.

Table 4.2: Initial Nose Cone Parameters

Parameter	Value
Diameter	144 in (3.6576 m)
Radius	72 in (1.8288 m)
Initial Length	525.6 in (13.35024 m)
Fineness Ratio	3.65

4.3 Nose Cone Geometry

The types of nose cone shapes can be described as Conical, Biconic, Power series, Ogival, Elliptical, and Parabolic. In subsonic flow, the air can respond to the approaching craft since the pressure field around it extends forward. This means that a suction area on one side of the fuselage or wing will start pulling molecules in before they reach the craft itself which causes the suction. A rounded or blunt nose allows the flow to approach from a range of angles without causing significant drag. The profile of an elliptical nose cone is one-half of an ellipse, with the major axis being the centerline and the minor axis being the base of the nose cone.



Fig 4.3: Elliptical Nose Cone

In supersonic flow, the air has no indication of the approaching craft. The first contact will cause a sudden change in direction, called a shock. In order to decrease the drag in supersonic flow, it is important to make the shock as weak as possible, which means that the sudden displacement in direction should be as small as possible. This can best be achieved by a slender, pointy tip. From “THE DESCRIPTIVE GEOMETRY OF NOSE CONES” by Gary A. Crowell Sr., in the transonic region from 0.8 to 1.2 Mach, either the Von Karman shape, or Power Series shape with $n = \frac{1}{2}$, would be preferable to the conventionally popular Conical or Ogive shapes. The Power Series includes the shape commonly known to modelers as a ‘parabolic’ nose cone. The Power Series shape is characterized by its (usually) blunt tip, and by the fact that its base is not tangent to the body tube.

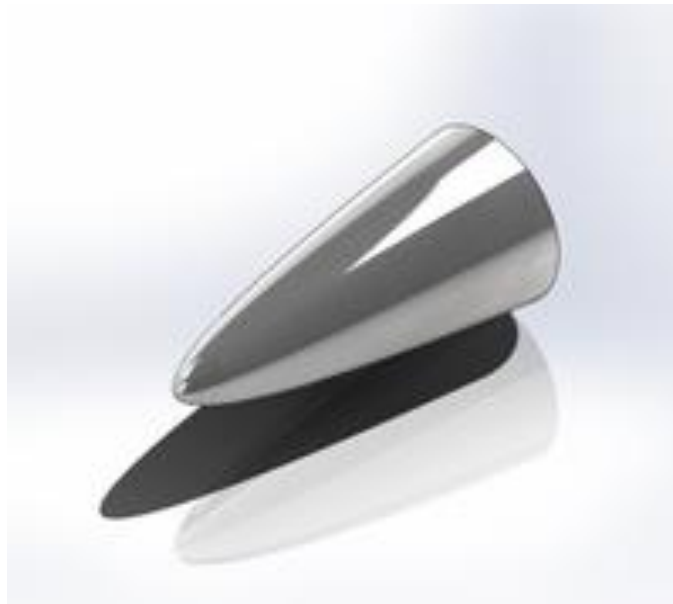


Fig 4.4: $\frac{1}{2}$ Power Series Cone

For the conceptual nose cone, it was decided that the nose cone would start off as an elliptical nose cone, then gradually morph into a nose cone of the $\frac{1}{2}$ power series profile.

Upto Mach 0.3, the nose cone retains its initial shape, that of an elliptical nose cone, beyond which it starts morphing gradually until Mach 0.8, beyond which it is constant, ie the nose cone assumes the profile of a $\frac{1}{2}$ power series nose cone from Mach 0.8 to Mach 1 and beyond (transonic range).

The tip of the nose cone is fixed, and the arc length is also fixed. The reason for keeping the nose cone fixed is so that the fixed section will impart the extension to the changes in ribs, keeping the arc length fixed. In the mechanism, aerodynamic heating is also taken into account, and a titanium tip could be utilised because the aerodynamic heating at the nose tip is particularly high.

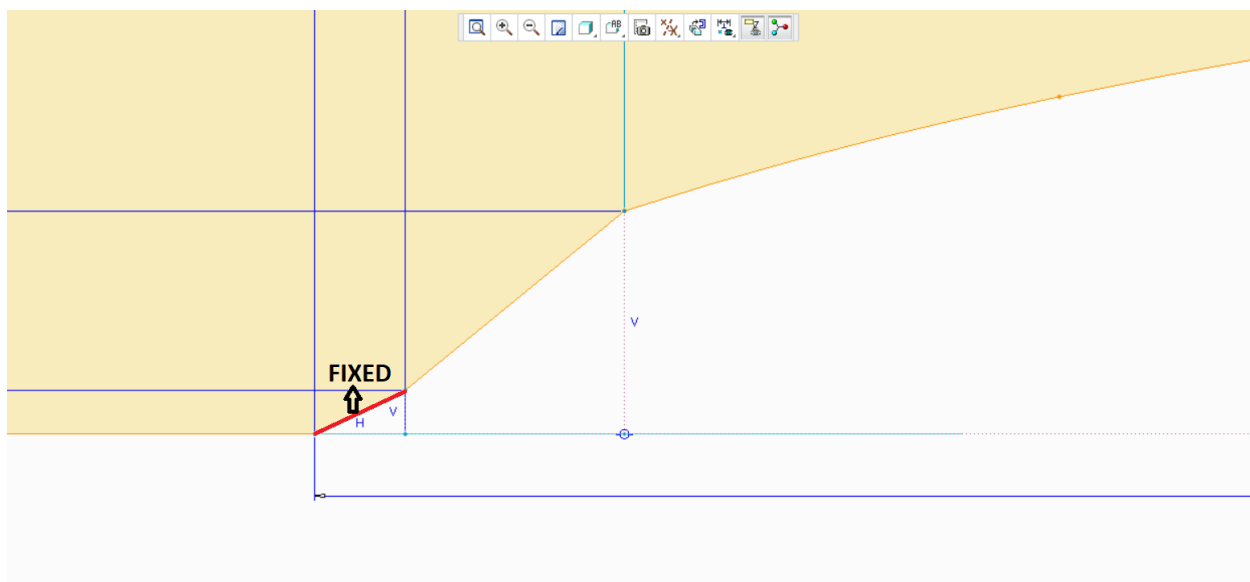


Fig 4.5: Fixed Parameter Geometry

Table 4.3: Fixed Parameters

Parameter	Value
Radius (Vertical Length)	5.12 in
Fixed Length (Horizontal Length)	10.4 in
Arc Length (Curve Length)	11.5898 in

The nose cone, which is built of active materials like SMA, morphs as a result of the ribs reducing in radius. With the decrease in width, and a simultaneous increase in length, the nose cone curvature reduces, allowing the nose cone to morph from an elliptical shape to the $\frac{1}{2}$ power series. Denoting Linear change of nose cone over mach number and time.

Table 4.4: Change in radius of the ribs

	Phase 1	Phase 2	Phase 3	Phase 4	Phase 5	Phase 6
Time of Flight	T = 27s	T = 33s	T = 38s	T = 43s	T = 48s	T = 53s
Mach no.	0.3	0.4	0.5	0.6	0.7	0.8
Time Difference for Morphing	t = 0s	t = 6s	t = 11s	t = 16	t = 21s	t = 26s
Rib Placements at X	Change in Radius of the Ribs Y _{0.3}	Change in Radius of the Ribs Y _{0.4}	Change in Radius of the Ribs Y _{0.5}	Change in Radius of the Ribs Y _{0.6}	Change in Radius of the Ribs Y _{0.7}	Change in Radius of the Ribs Y _{0.8}
0	72	72	72	72	72	72
40	71.79119448	71.20057772	70.70839709	70.21621646	69.72403583	69.2318552
90	70.93660199	69.70684076	68.68203974	67.65723872	66.6324377	65.60763668
140	69.39885563	67.63861445	66.17174679	64.70487913	63.23801147	61.77114381
190	67.13102555	64.95002771	63.13252951	61.3150313	59.4975331	57.68003489
240	64.05561479	61.56793875	59.49487539	57.42181202	55.34874865	53.27568528
290	60.04866982	57.37731172	55.15117998	52.92504823	50.69891648	48.47278473
340	54.90662505	52.19088488	49.92776807	47.66465126	45.40153445	43.13841765
390	48.26806364	45.67782458	43.51929203	41.36075949	39.20222694	37.04369439

440	39.38334961	37.15439057	35.2969247	33.43945884	31.58199297	29.7245271
490	26.04734636	24.62205359	23.43430961	22.24656564	21.05882166	19.87107769

Table 4.5: Change in length of nose cone for different phases

Mach no.	0.3	0.4	0.5	0.6	0.7	0.8
Change in length	0	1.348731494	2.323688015	3.188127738	3.940253342	4.591716075
Nose length	525.6	526.9487315	527.923688	528.7881277	529.5402533	530.1917161
Overall Falcon9 length	2754.6	2755.948731	2756.923688	2757.788128	2758.540253	2759.191716

The Geometry of each phase transformation from elliptical to $\frac{1}{2}$ power series profile linearly is shown below



Fig 4.6: Phase 1

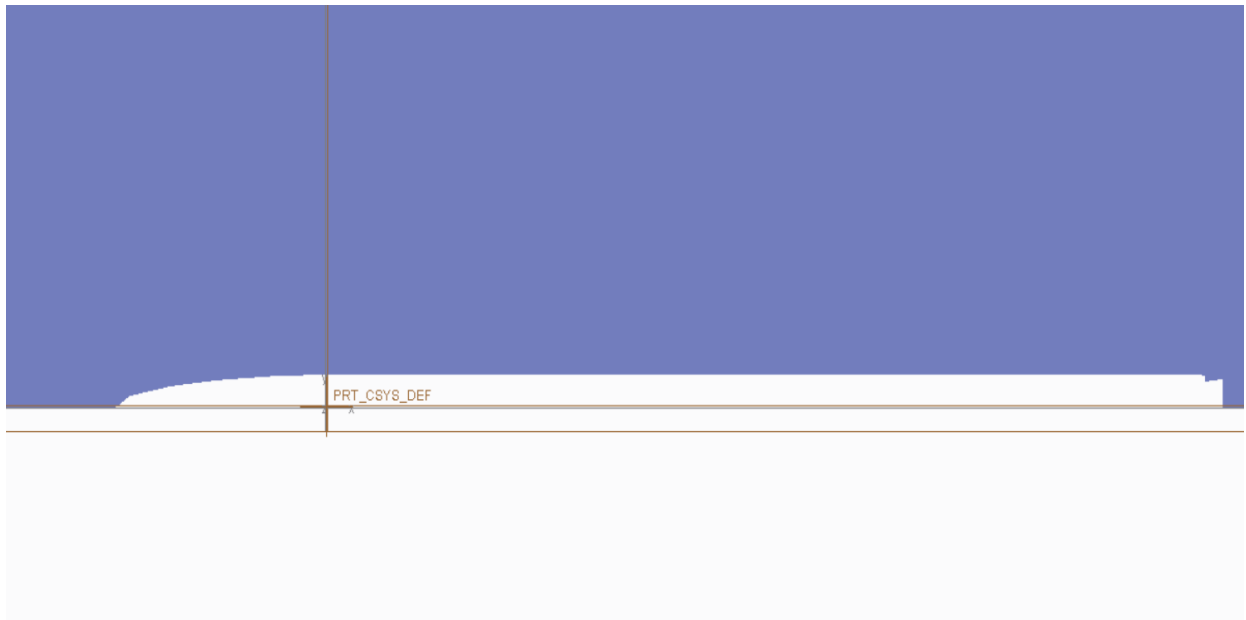


Fig 4.7: Phase 2

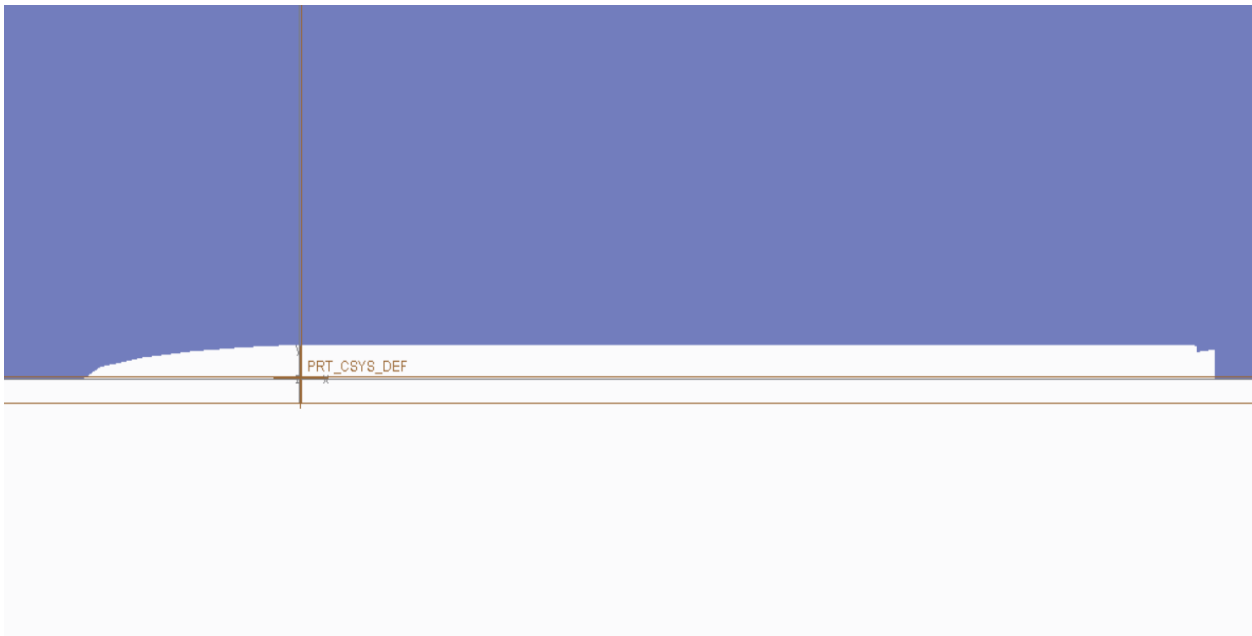


Fig 4.8: Phase 3

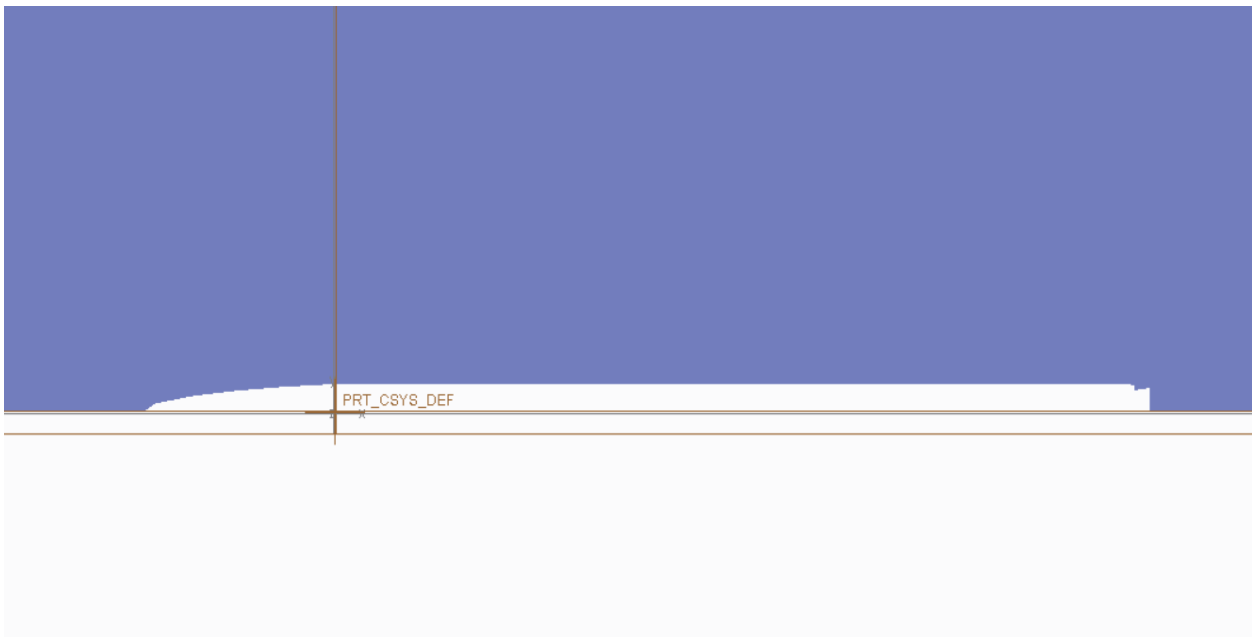


Fig 4.9: Phase 4



Fig 4.10: Phase 5

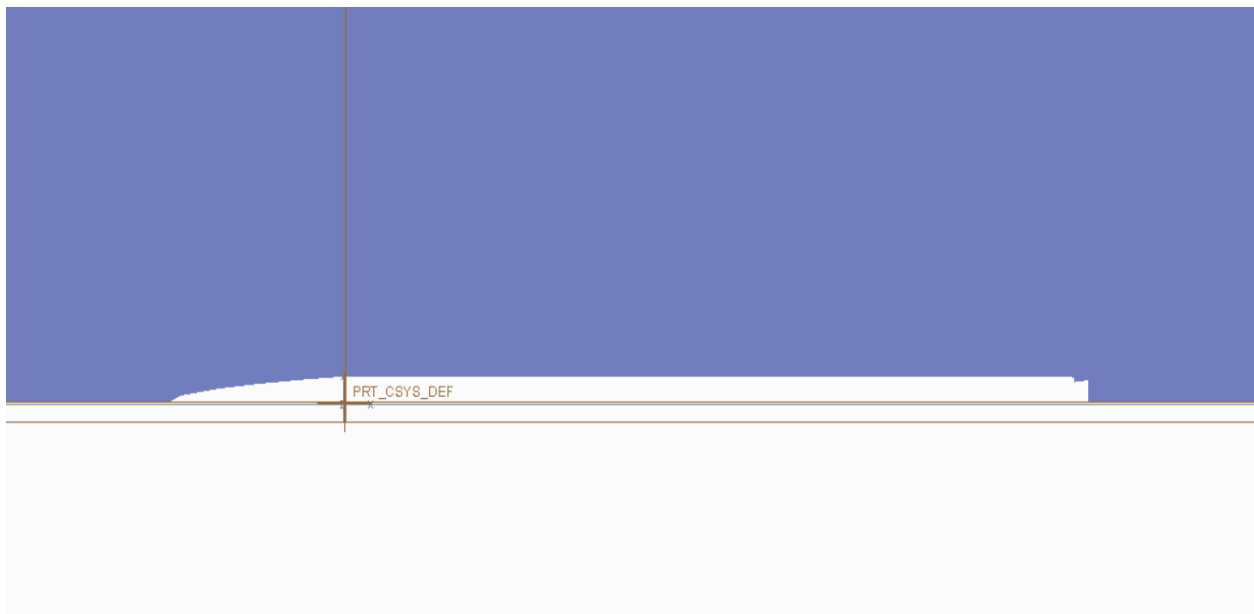


Fig 4.11: Phase 6

The above geometries will be used to calculate the impact of morphing nose cone instead of using an individual nose cone.

5. SETUP

Ansys Fluent will be used to run the simulations for each nose cone geometry. The setup needs for the simulations, such as computational domain, meshing, and Fluent settings, will be covered in the following sections.

5.1 Computational Domain

The computational domain was the first element of the setup. The rectangular domain and the bullet shaped domain were the two computational domains that were most commonly employed in the reference literature. The computational domain was originally constructed using rectangle geometry. When meshing, however, this proved challenging because the meshing resulted in a high element count in non-essential regions and poor mesh quality. The bullet-shaped computational domain, the second alternative, was significantly easier to mesh and complimented the curvature of the nose cone profile, resulting in higher mesh quality. Below is a picture of the completed computation domain. The domain was halved and rendered axisymmetric, because the nose cone angle of attack was continuously zero. Furthermore, the domain was extended two times from the rocket's end, and the outlet was positioned there, with the nose cone attached to the rocket.

In Creo Parametric's generative shape design, the computational domain was sketched. The basic shape of the domain was drawn out as shown in the diagram below. A line of length L connects the outlet at the top of the domain. An oval was used to connect the lines and axis. The vertical distance between the nose cone and the top of the domain was initially smaller, but after preliminary simulations revealed that shockwaves were reflected, the distance was increased.



Figure 5.1: Computational Domain

5.2 Meshing

The computational domain meshing procedure was an iterative process. When it came to iterating on the mesh, there were two key objectives that needed to be met. The first goal was to verify that all of the major simulation characteristics, such as shockwaves, boundary layers, and so on, were recorded. The mesh's second purpose was to guarantee that the flow transitioned smoothly to avoid numerical errors. Because the epidemic limited access to extra computing capacity, the second goal was hampered; as a result, the element count was kept within reasonable bounds. The geometry of the computational domain was separated into several faces to fulfil these goals, which helped to generate a more progressive mesh. These divisions were determined after a series of iterations in which different cuts were examined to see how the mesh developed and what improvements were required. A mixture of structured and unstructured pieces were used to form the final mesh.

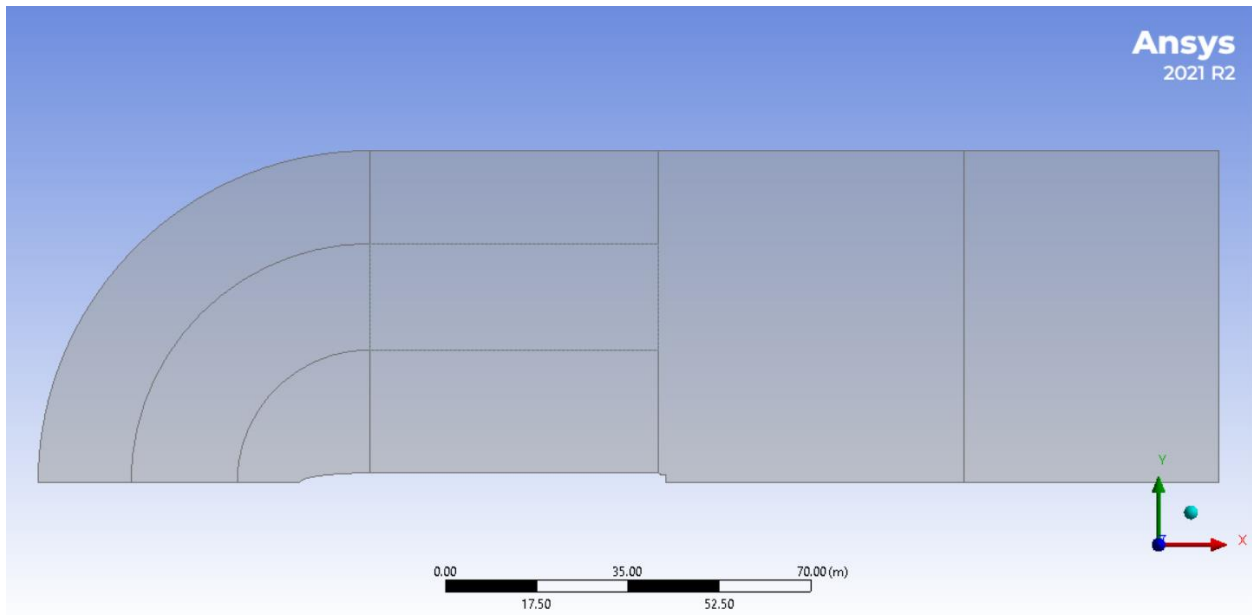


Figure 5.2: Split Face Geometry For Meshing

The splits in the geometry can be noticed in the figure. Faces were mostly made up of organised pieces, which helped to reduce the amount of computational power required in areas where phenomena were rare. The unstructured mesh was used for the rest of the faces. Due to their proximity to the nose cone profile, these areas were meshed more densely in order to capture all important flow patterns. Faces 3 and 4 were meshes, and each pair represented a level of the mesh. The elements would cross the levels and get finer as they got closer to the nose cone profile. It was made sure that as the elements were finer, the transitions would be gradual in order to reduce the number of numerical errors.

The grid convergence study produced the finest mesh, as shown in the image below. It was also the mesh that all simulation runs were based on.

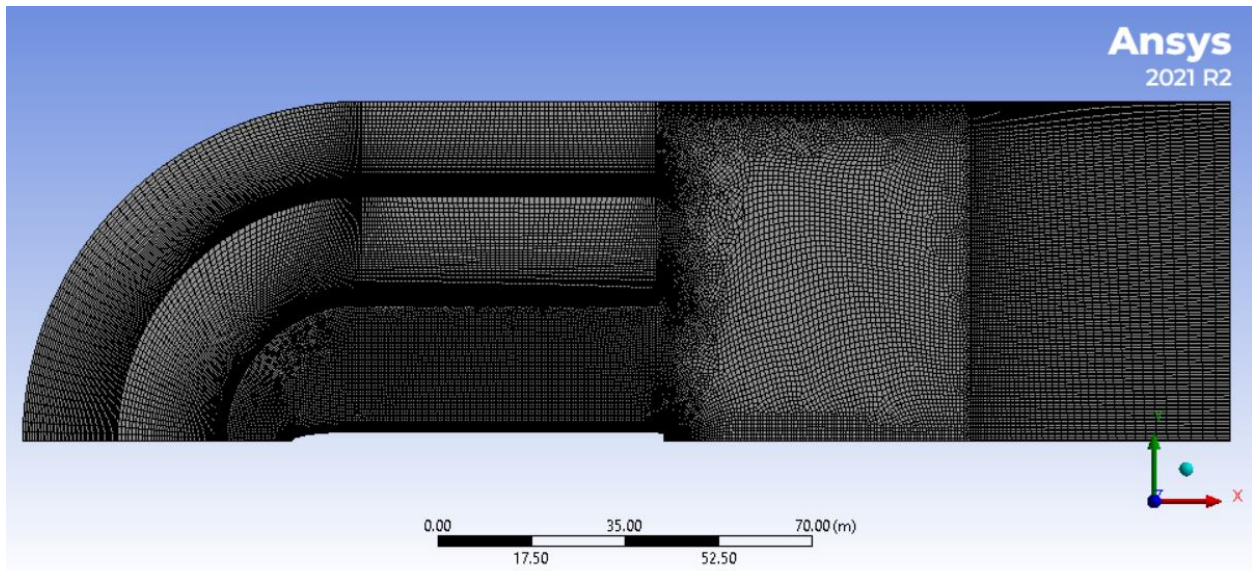


Figure 5.3: Nose Cone Mesh

The incremental steps of mesh granularity increase are depicted in Fig. 5.4 below.

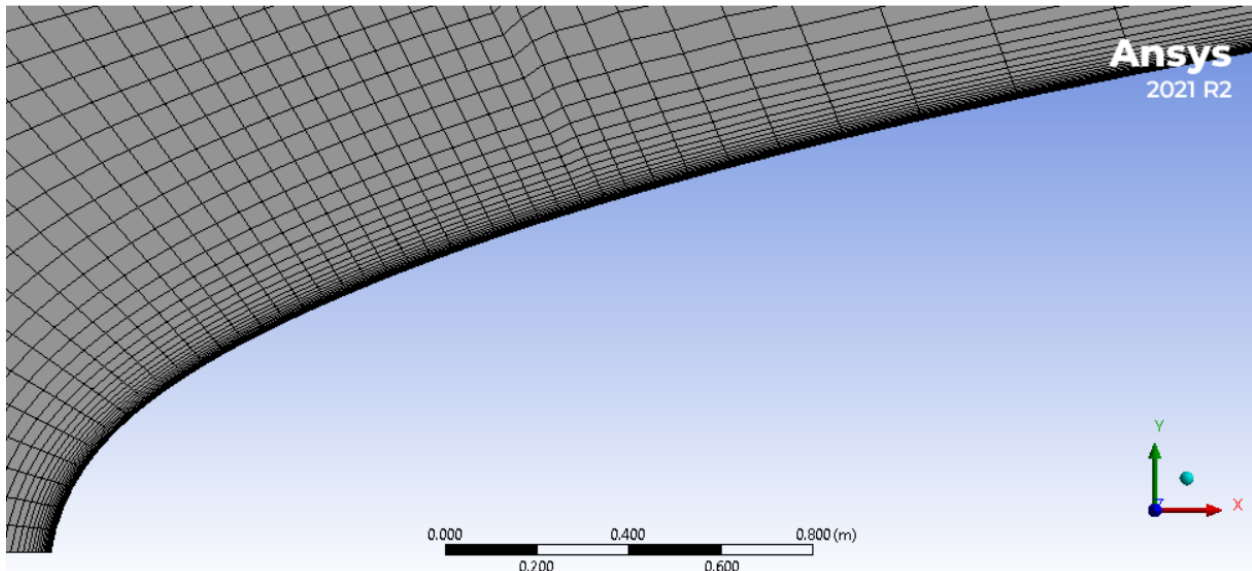


Figure 5.4: Mesh Granularity

The final figure below displays the inflation layer which represents the boundary layer. Additionally, a sphere of influence was added to the apex of the nose cone profile to increase the local mesh quality and helped to predict the flow more accurately at the nose.

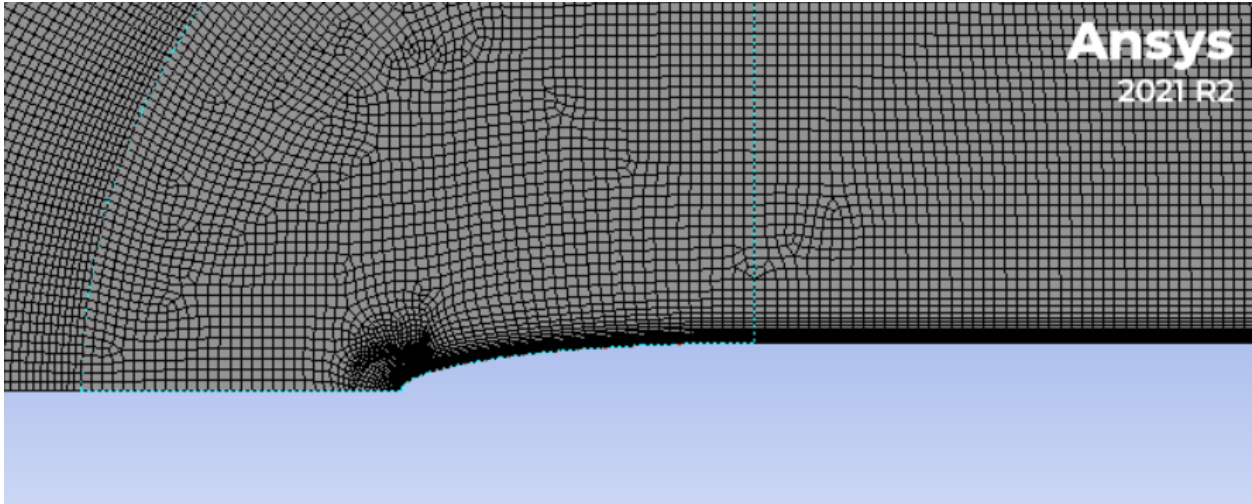


Figure 5.5: Meshing at Nose Cone Apex

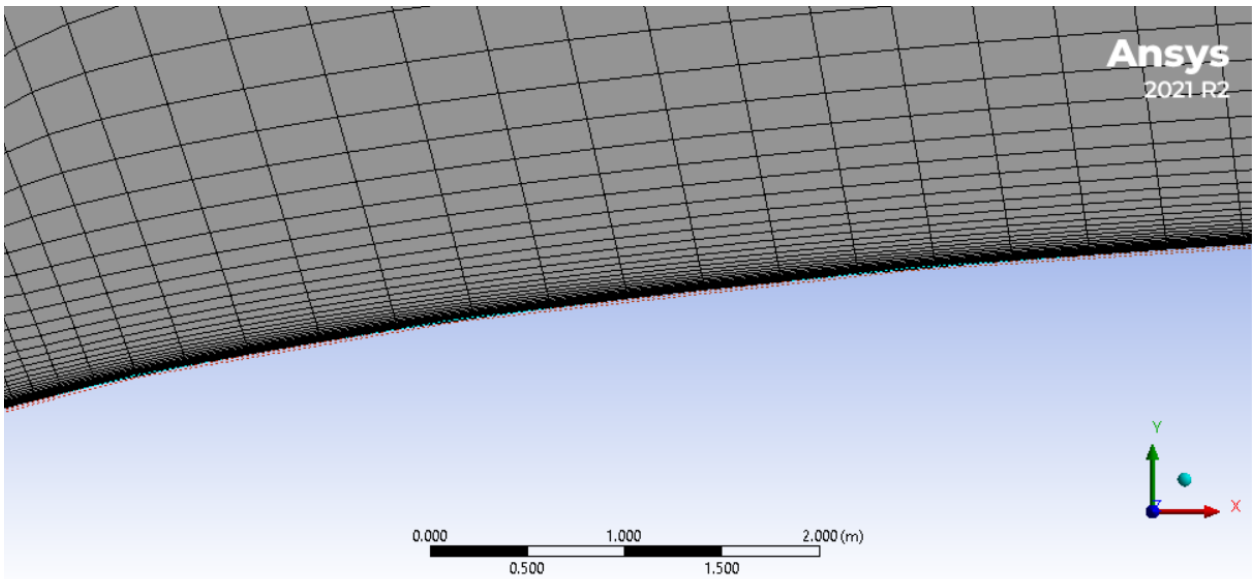


Figure 5.6: Boundary Layer at Nose Cone

5.3 Fluent Settings

The simulations were then run using Fluent's process after the meshing was completed. Fluent workflow may be split down into a few simple tasks. The initial set of duties involved configuring the overall settings. To account for compressibility effects, a density-based solver was chosen because the starting Mach number was 0.3. Since the computational domain was half, the planar space was set to axisymmetric. The default settings for the other general parameters were kept alone. Setting up the material properties was the second set of responsibilities. Because the flow was compressible, it was necessary to alter the fluid's density and viscosity, which in this case was air. The viscosity was set to Sutherland's Law, while the density was set to an ideal gas (3 coefficient method). Both of these options make density and viscosity temperature dependent, which is necessary for compressible flow.

The viscous solver chosen was the k SST model, which predicts flow separation better than most RANS models and accounts for its superior performance under adverse pressure gradients. The viscous solver and boundary conditions were the last two tasks to be completed. In adverse pressure gradient boundary layers, k SST can account for the transfer of the main shear stress. Because of its great accuracy-to-cost ratio, it is the most often used model in the business. The viscous solver and boundary conditions were the last two tasks to be completed. Furthermore, the model was created with wall-bounded flows in mind for aerospace applications. For boundary layers subjected to unfavourable pressure gradients, the model has been found to yield good results. The SST model creates some substantial turbulence levels in places with large normal strain, such as standstill zones and regions with rapid acceleration, which is one of the model's disadvantages. Because the model is resource-conserving, it is an excellent choice for low-resource computing environments.

Setting up the boundary conditions was the last set of duties. It's worth noting that named choices of the boundary conditions should be generated before the meshing is uploaded to Fluent. The Fluent settings part of the Appendix contains this process, illustrations, and exact values. Pressure far-field outlet, axis, and nose cone profile were the five boundary criteria that were defined (wall). The inlet was set to a pressure far-field determined in Mach no and moved along the x-axis in a positive direction. The pressure farfield was configured, with a gauge pressure of zero adjusted to 101325 Pa, the atmospheric operating pressure.

The velocity of the freestream was represented by the pressure far-field, which was entered as a Mach number rather than a velocity. The axis indicated the line of symmetry, as the computing domain had been divided in half. Finally, in the computational domain, the nose cone profile was depicted as a cut out. The length and cross-sectional area of the nose cone had to be inserted as well, thus setup for the wall was also required in the references section. The computational domain and boundary conditions are represented in the diagram below.

5.4 Boundary Conditions:

Table 5.1: Boundary Conditions

Mach No. Inlet	0.3, 0.4, 0.5.....1.0
Temperature	300 K
Gauge Pressure	0 Pa
Operating Pressure	101325 Pa
Axial Component of Flow Direction	1
Radical Component of Flow Direction	0

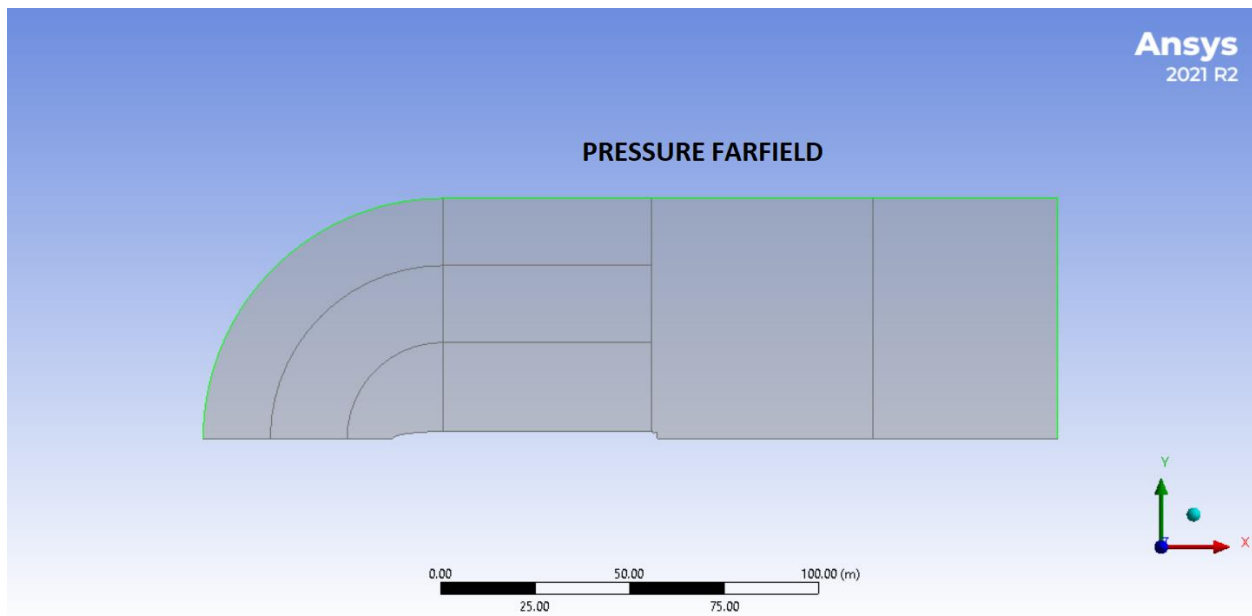


Figure 5.7: Boundary Conditions-1

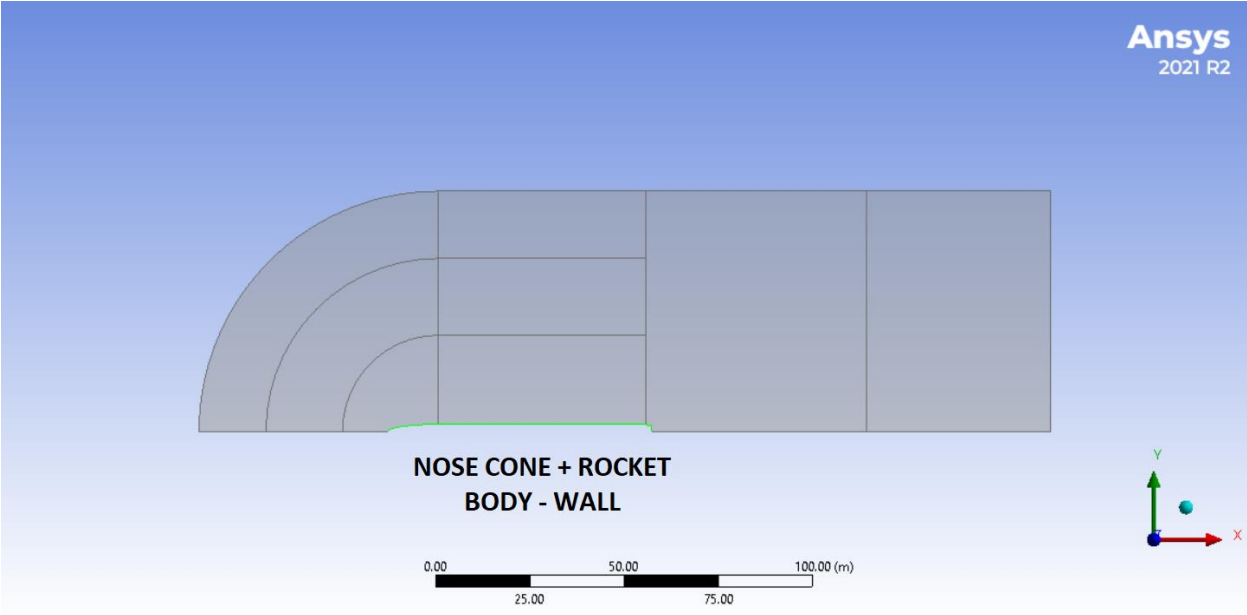


Figure 5.8: Boundary Conditions-2

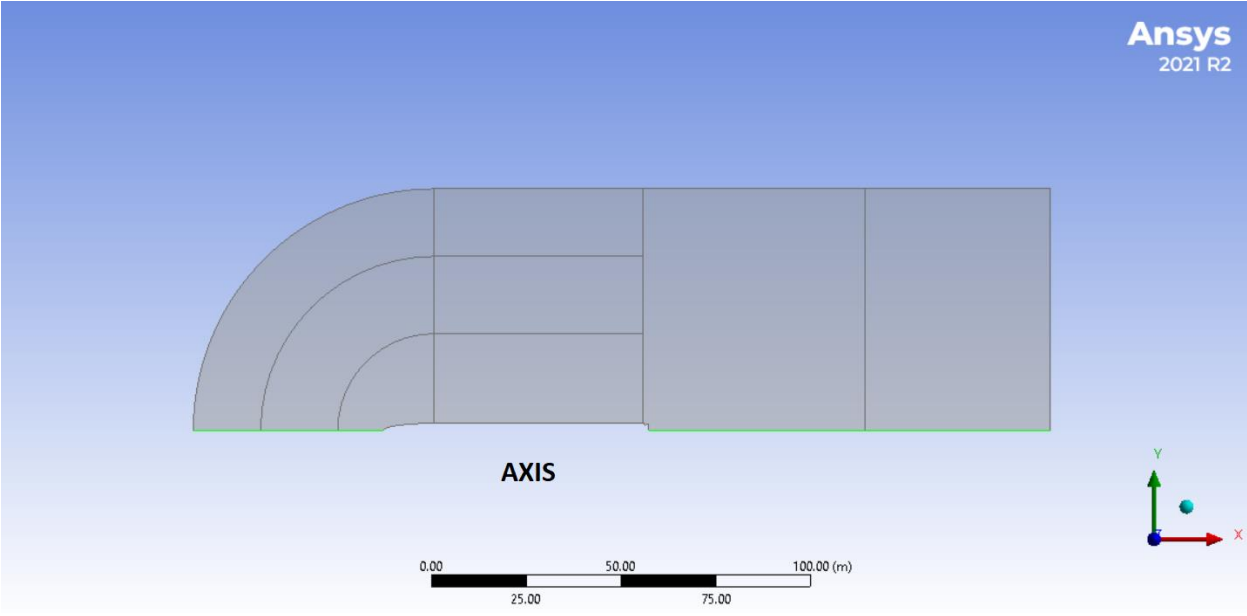


Figure 5.9: Boundary Conditions-3

5.5 Fluent Setup

This section includes images of the precise Fluent settings so that the study can be easily replicated in the future.

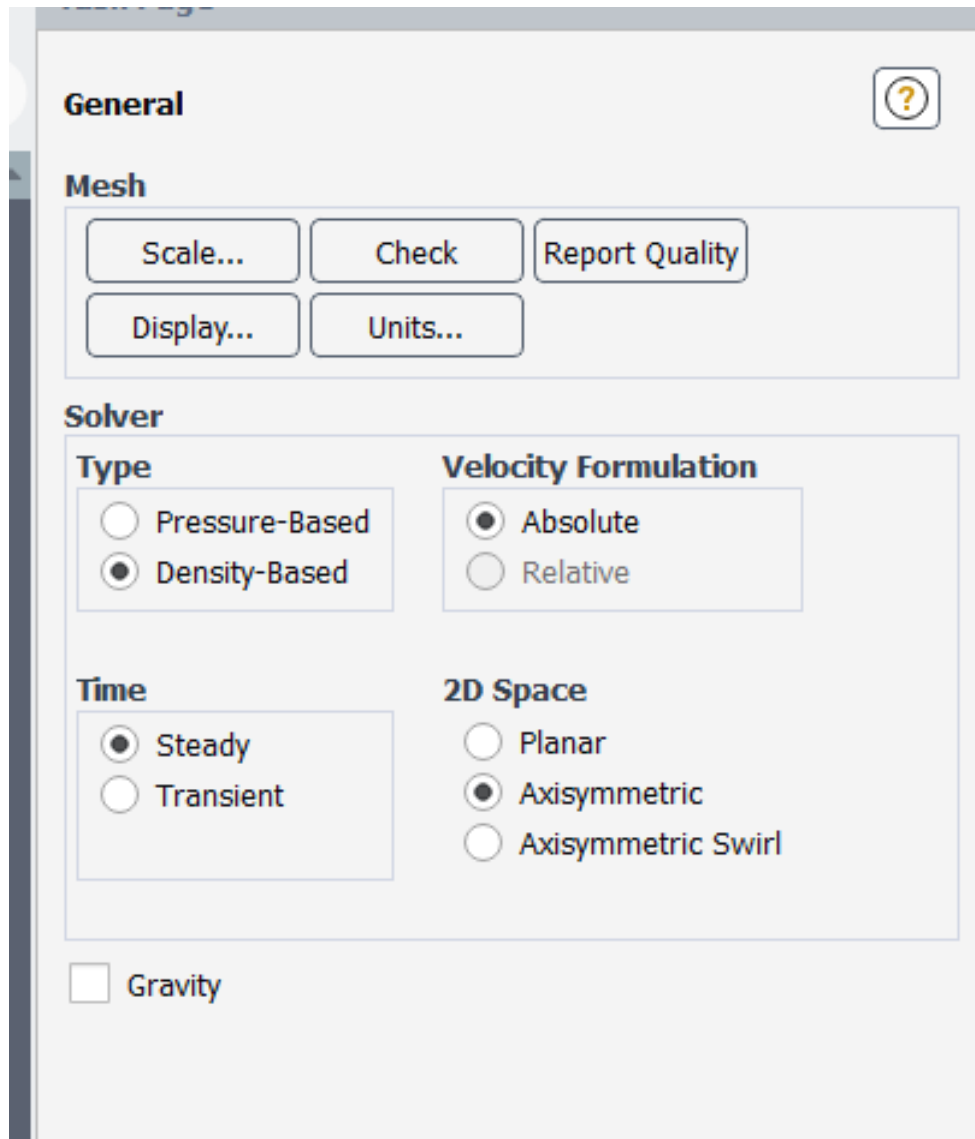


Figure 5.10: Fluent General Settings

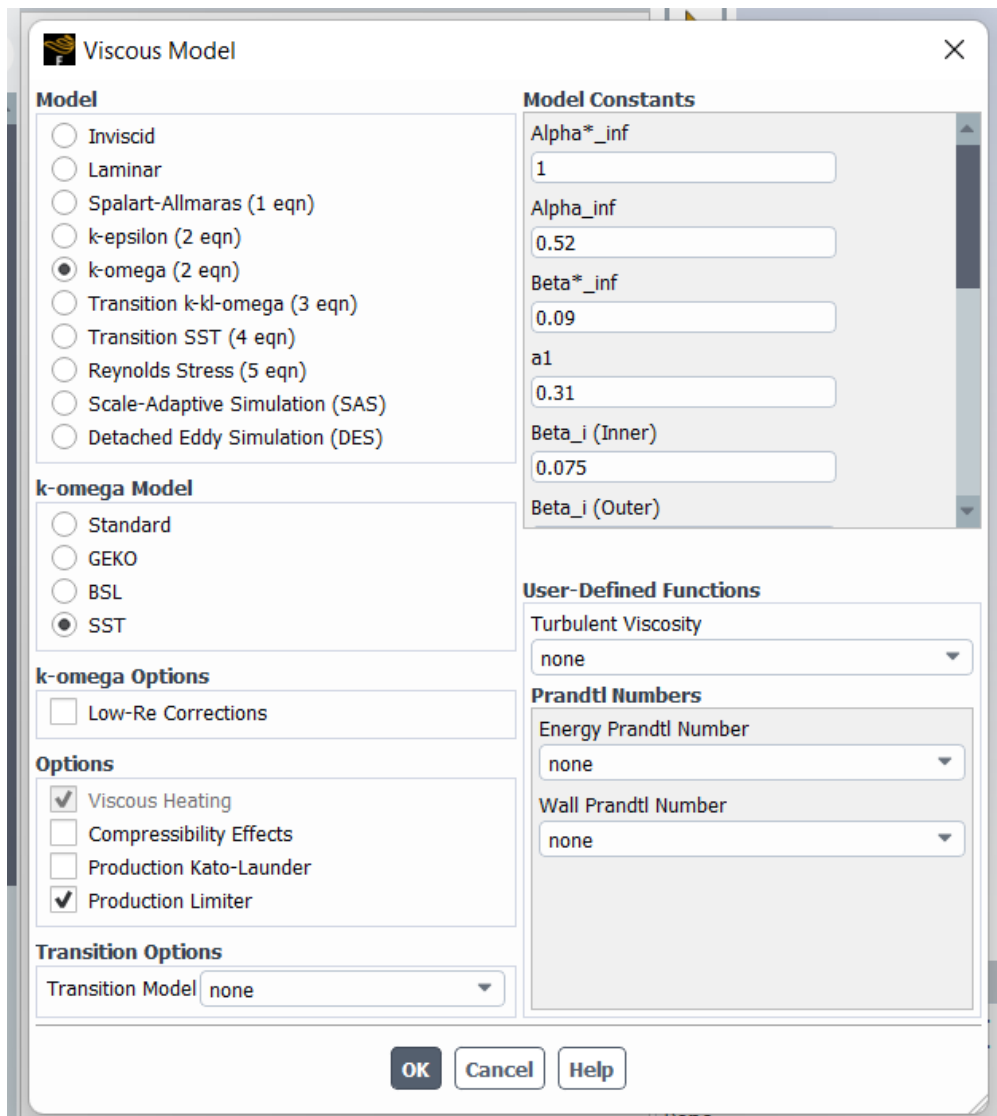


Figure 5.11: Fluent Viscous Model

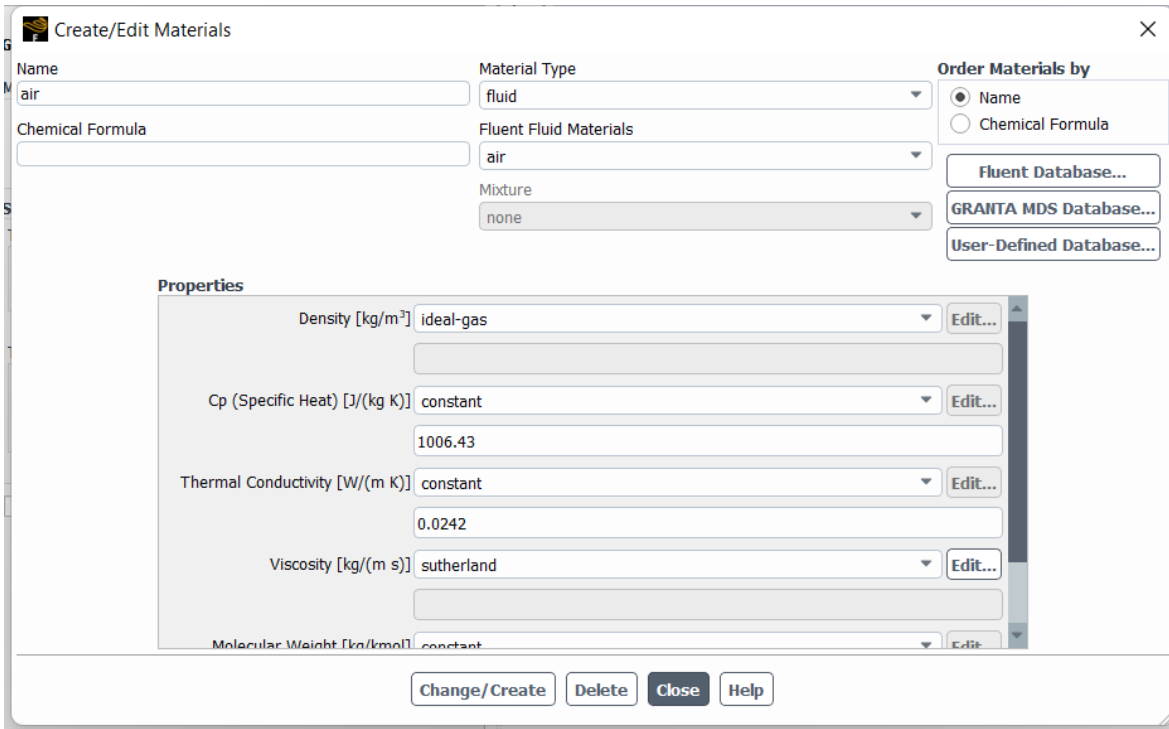


Figure 5.12: Fluent Material Properties

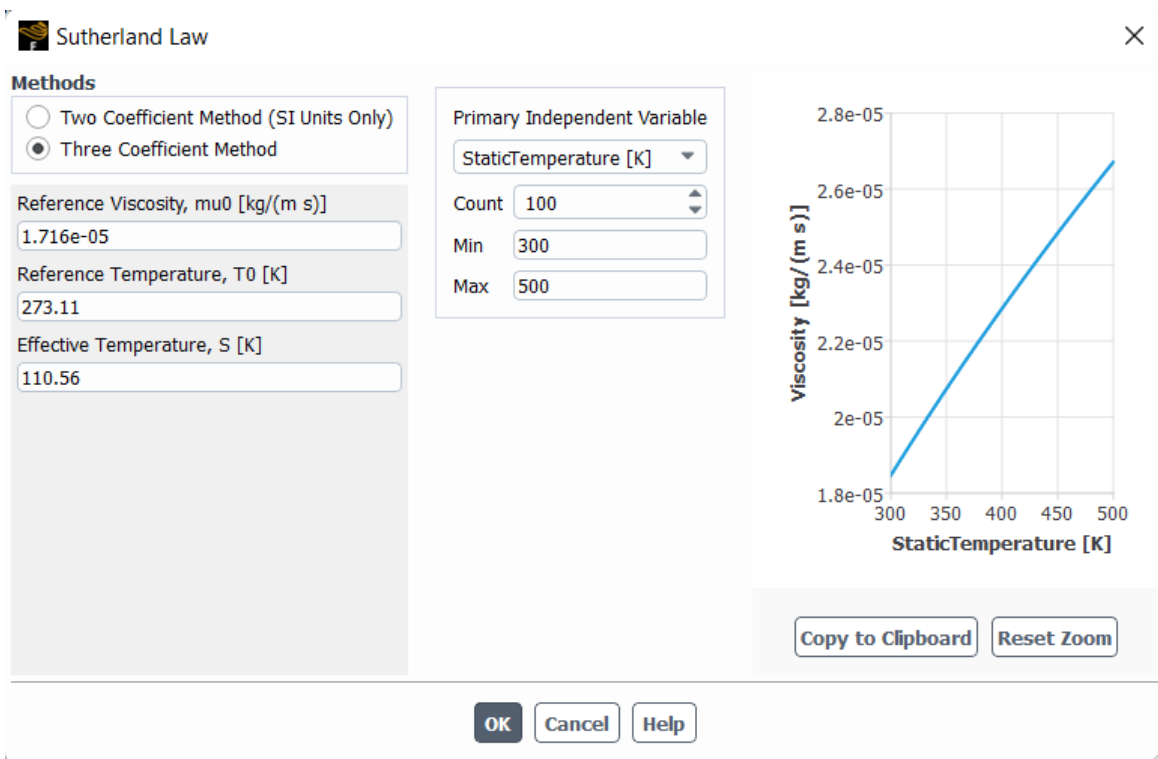


Figure 5.13: Fluent Material Properties Sutherland's Law

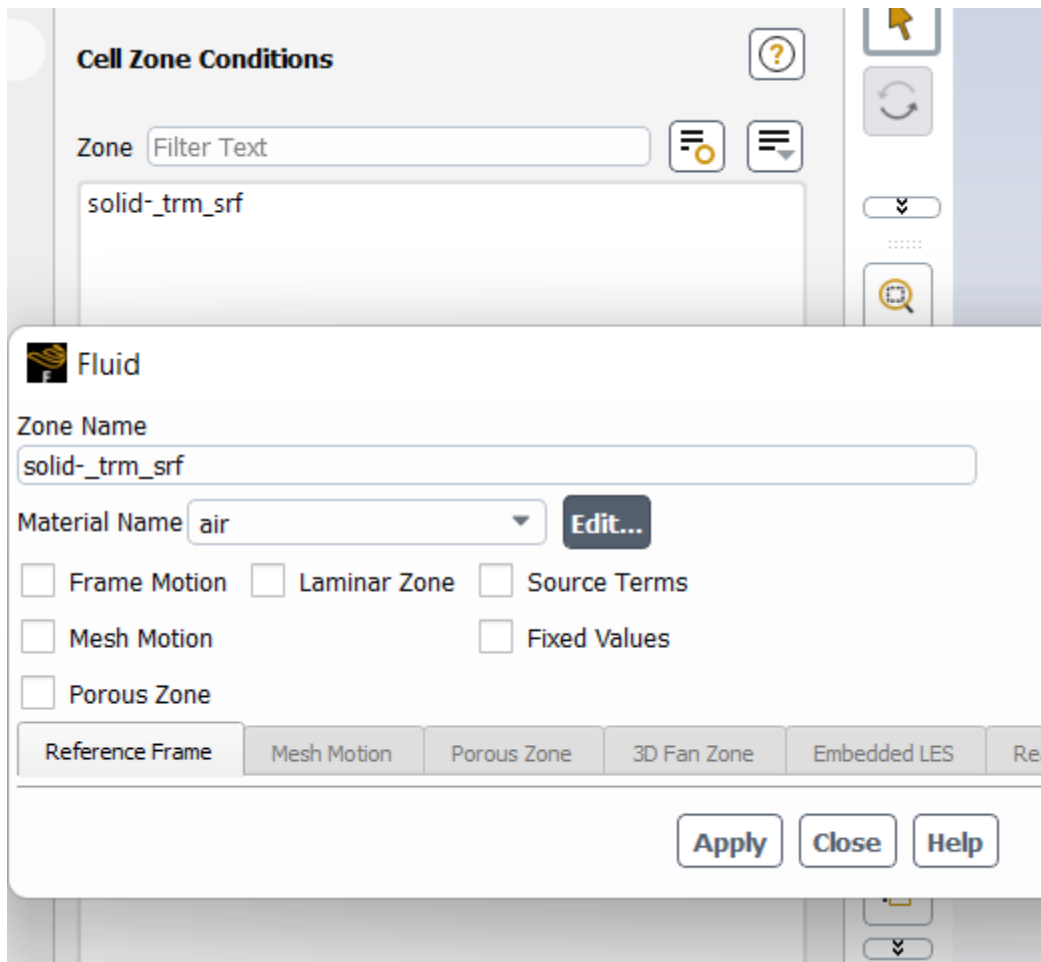


Figure 5.14: Fluent Cell Zone Conditions

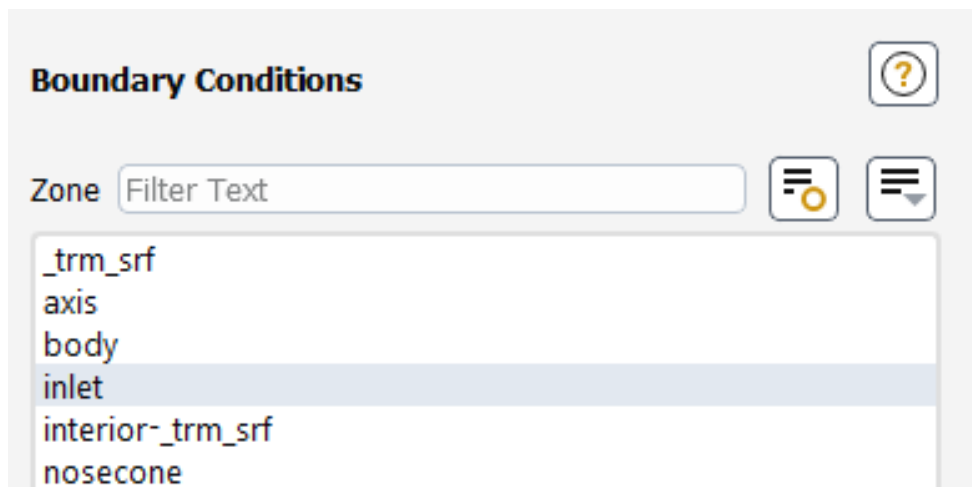


Figure 5.15: Fluent Boundary Conditions

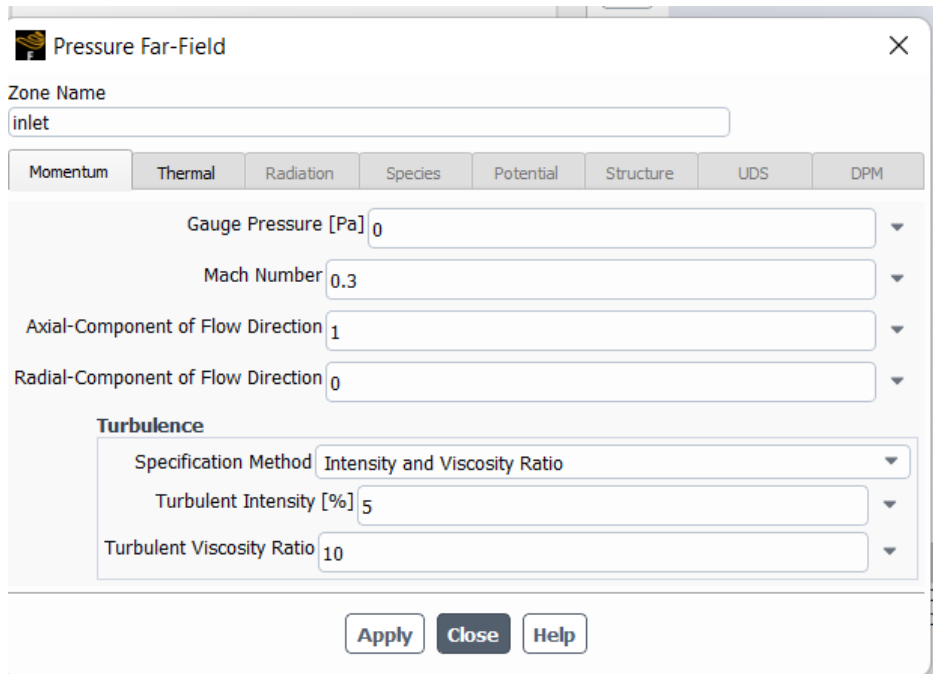


Figure 5.16: Fluent Boundary Conditions - Inlet

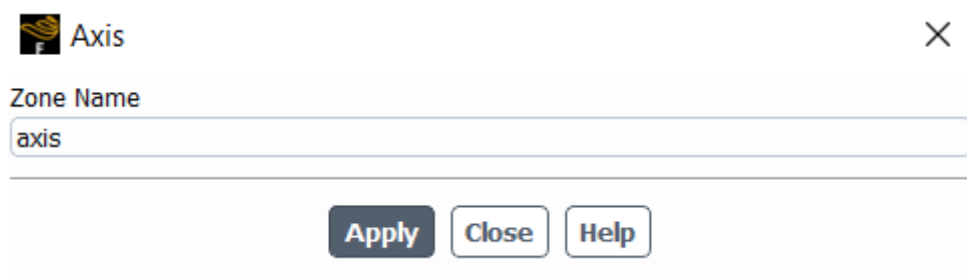


Figure 5.17: Fluent Boundary Conditions - Axis

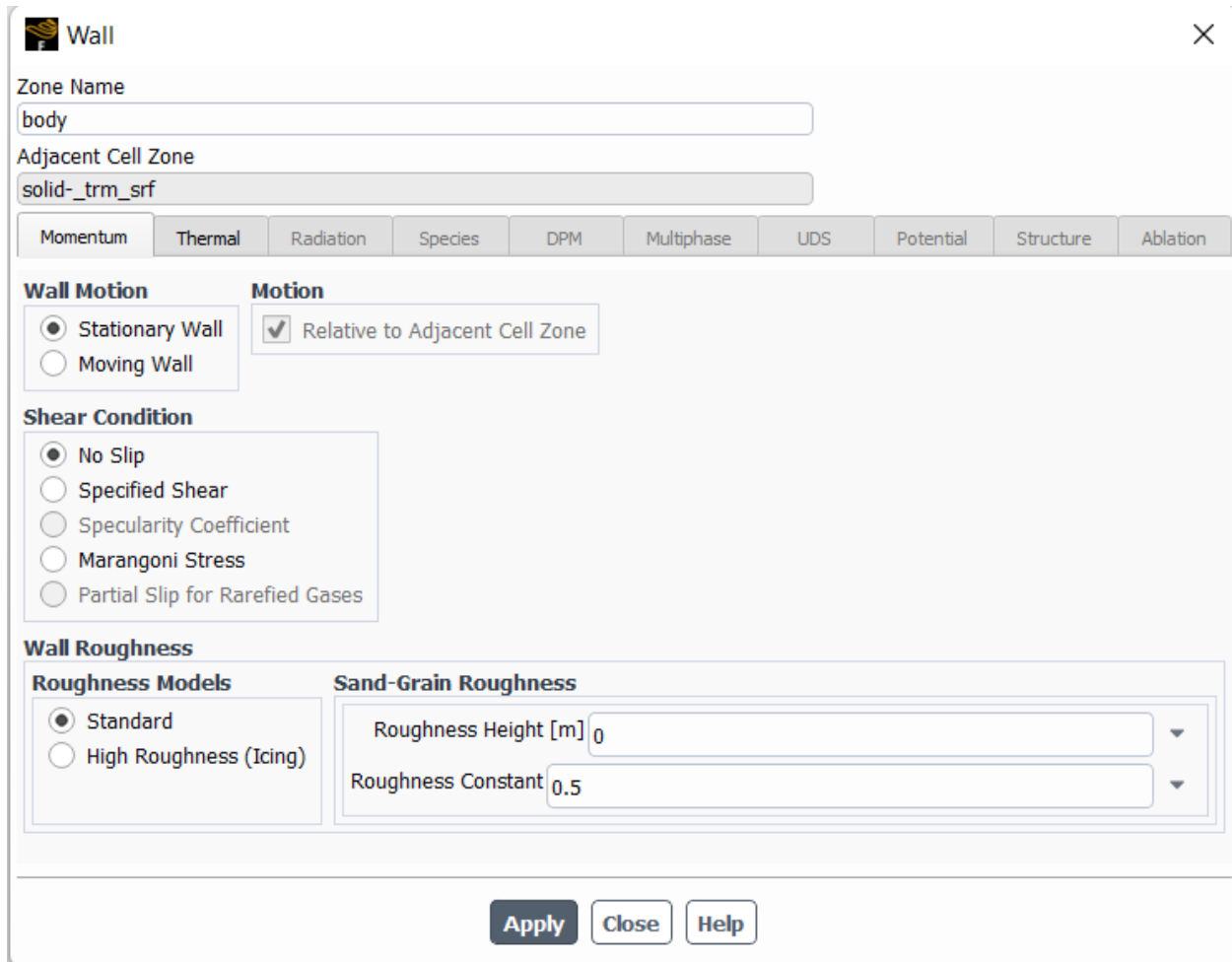


Figure 5.18: Fluent Boundary Conditions - Body

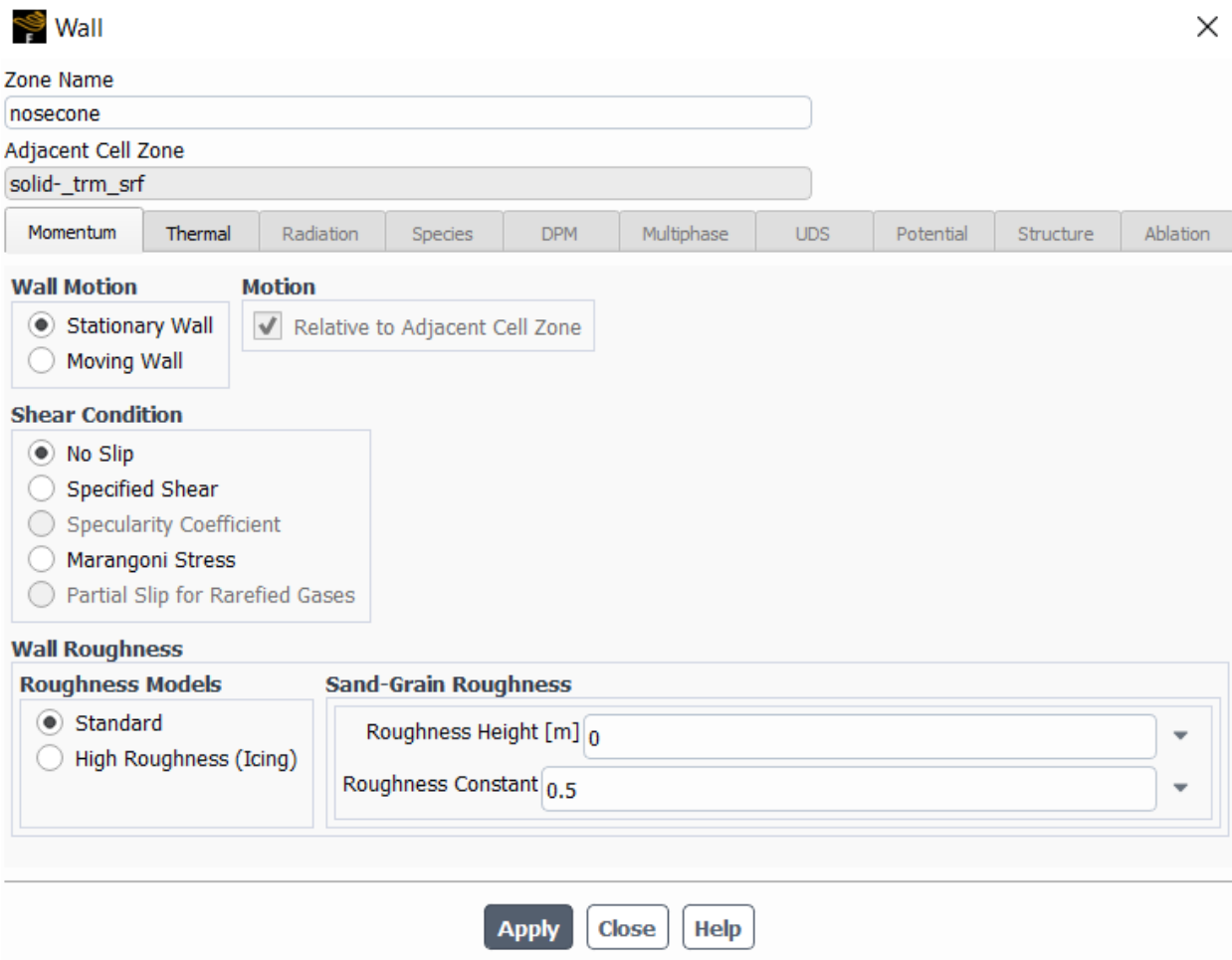


Figure 5.19: Fluent Boundary Conditions - Nose Cone

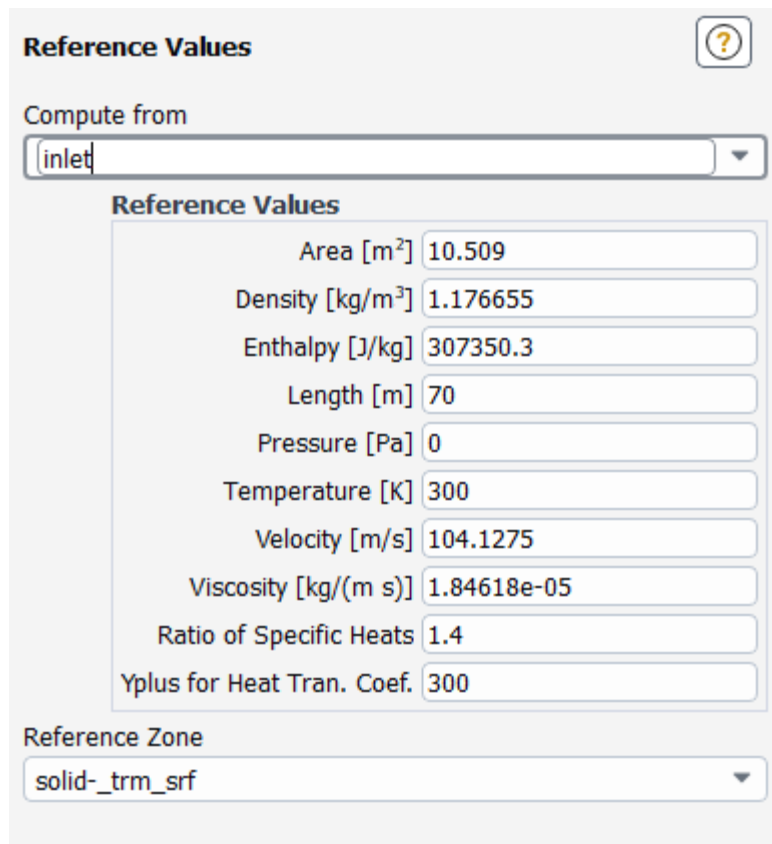



Figure 5.20: Fluent Reference Values

Solution Controls 

Courant Number

Under-Relaxation Factors

Turbulent Kinetic Energy

Specific Dissipation Rate

Turbulent Viscosity

Solid

Figure 5.21: Fluent Courant Number

Solution Initialization ?

Initialization Methods

Hybrid Initialization
 Standard Initialization

Compute from
inlet

Reference Frame

Relative to Cell Zone
 Absolute

Initial Values

Gauge Pressure [Pa]	0
Axial Velocity [m/s]	104.1275
Radial Velocity [m/s]	0
Turbulent Kinetic Energy [m ² /s ²]	40.65949
Specific Dissipation Rate [s ⁻¹]	265790
Temperature [K]	300

Initialize Reset Patch...

Reset DPM Sources Reset LWF Reset Statistics

VOF Check

Figure 5.22: Fluent Initialization

6. VALIDATION

This section looks at validating the data acquired from the simulations. While it is very important to validate data through experimental means, due to the pandemic and financial issues this was not possible. Therefore, validation was attempted through other means such as: Y^+ values, flow development, and a mesh independence study using the grid convergence index.

6.1 Y^+ Values

Following the comparison investigations, another metric, the y^+ values, was examined. The y^+ value is a non-dimensional number that represents the distance from the wall in viscous lengths. The mesh must be able to capture the viscous effects of the flow in the case of the nose cone. According to the k-w model, the y^+ values should be less than 300, with 1 being the optimal number. Due to processing power constraints, a value of 1 for y^+ proved impossible to obtain at higher Mach numbers, so we set y^+ to 300.

Table 6.1: y^+ Plot

Free stream velocity U [m/s]	411.16
Density ρ [kg/m³]	1.204
Dynamic viscosity μ [kg*m/s = N*s/m² = Pa*s]	0.00001813
Characteristic length L [m]	70
Desired y^+ [dimensionless]	300
Kinematic viscosity ν [m⁴/s]	0.000015058139534883723
Reynolds number Re_x [dimensionless]	1911338378.3783784
First cell height [m]	0.00054678485087935
Boundary layer thickness [m]	0.3606054183668216

6.2 Mesh Independence Study

It was critical to verify that the simulation results were mesh independent after they had been calculated. A grid convergence index was developed to see if this was true. The drag coefficient was chosen as the pivotal variable for the grid convergence index. The mesh's grid size is calculated initially to begin the procedure. A 2D domain's grid size is calculated by dividing the domain's area by the number of elements and then taking the square root of that value. Three meshes with different element counts, node counts, and grid sizes were produced in total.

The grid refinement factor must be calculated after the grid size has been determined. The course grid size is divided by the fine grid size to arrive at this figure. The grid refinement factor should usually be more than 1.3.

The apparent order provided by the method was then calculated. The $q(p)$ is 0 since the grid refinement ratio was maintained constant. The initial mesh's inaccuracy was pretty little at first. Additional refining, on the other hand, reduced the inaccuracy by at least 1%.

Similarly, the relative error was minimal. This disparity can be explained by the fact that as mesh density increased, y^+ values decreased, making values near the end of the velocity profile more susceptible to change.

Table 6.2: C_d readings at different element quantity

Element	C_d
69124	2.21E-01
64493	2.21E-01
61856	2.21E-01
60552	2.20E-01
50835	2.19E-01
48086	2.19E-01
45372	2.17E-01

40665	2.11E-01
38403	2.09E-01
22061	1.68E-01
14005	1.13E-01

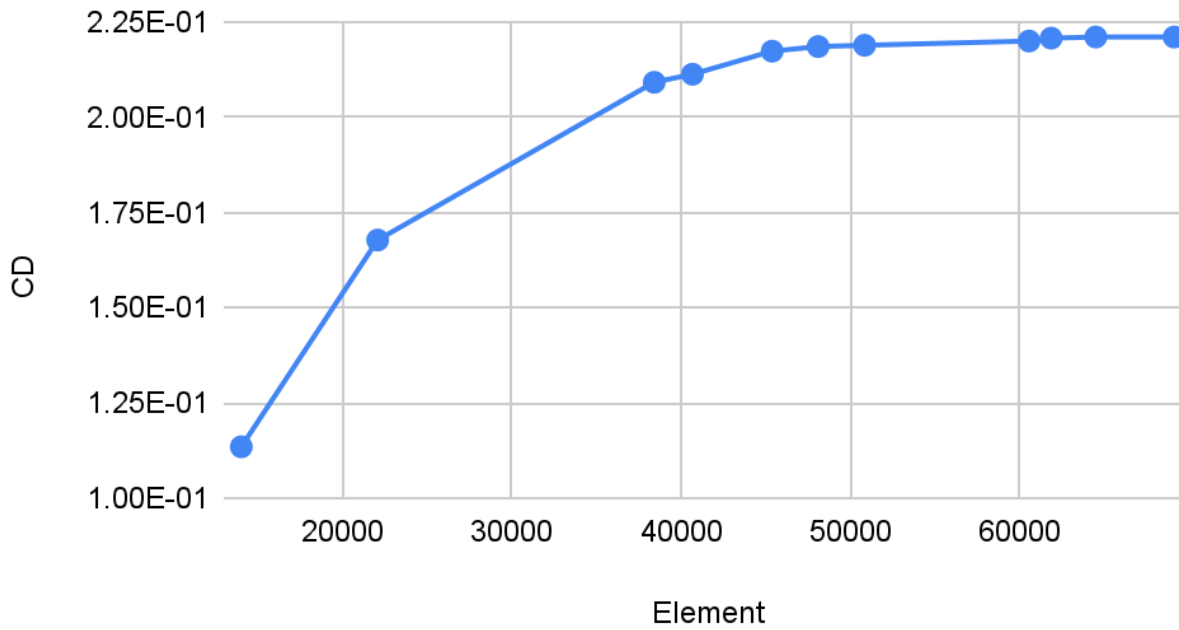


Fig 6.1: C_d vs Element Mesh Validation Graph

All of the Mach numbers had low values, indicating that changes in Mesh did not have a significant impact on the results.

7. ANALYSIS

This section will analyze the data acquired from the simulations after all the settings, setup, and validations in the preceding sections have been performed. The goal was to see if the Morphing nose cone was the best option given the requirements.

The accompanying plots and computationally generated contours assist us in understanding the flow interaction with different nose cone profiles, when looking at the subsonic flow regime that the vehicle passes through during initial.

The drag coefficient and drag force for a set of Mach values, as well as the phases to be evaluated, were the two most important data sets acquired. To obtain the data sets, the procedure was to run simulations on the various stages of transformations, ie to run simulations on each phase transformation model. This meant that the static elliptical nose cone and the static power series nose cone both had to undergo simulations from Mach 0.2 all the way to Mach 1.

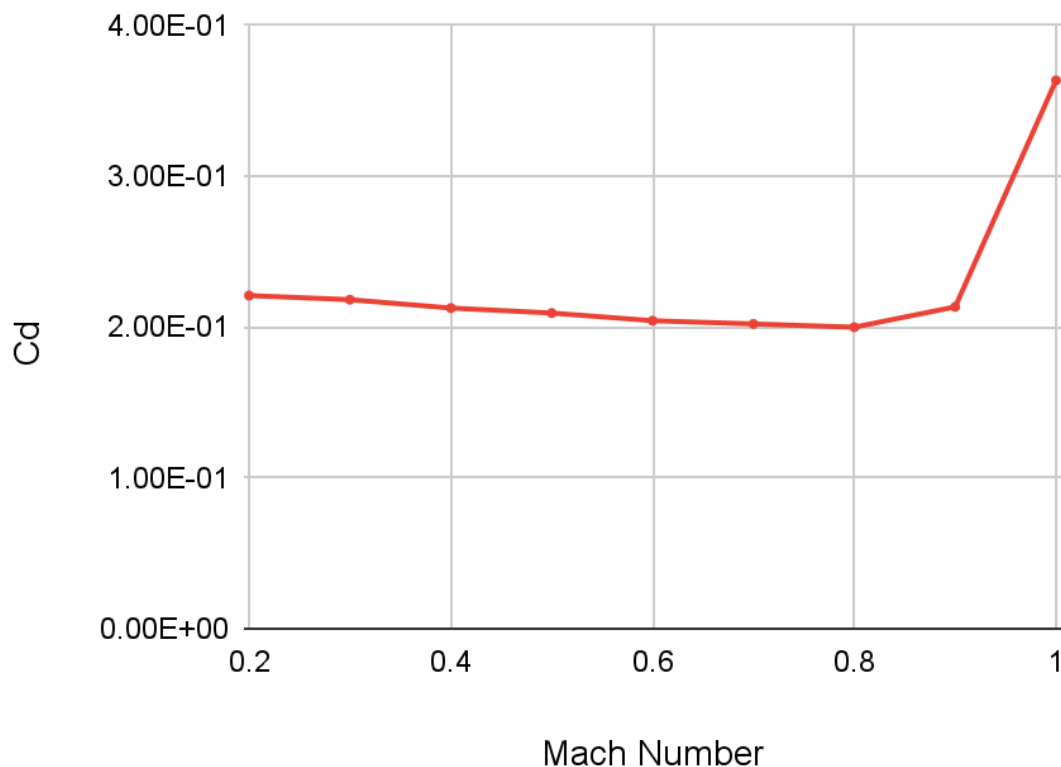


Fig 7.1: C_d vs Mach number for Ellipse

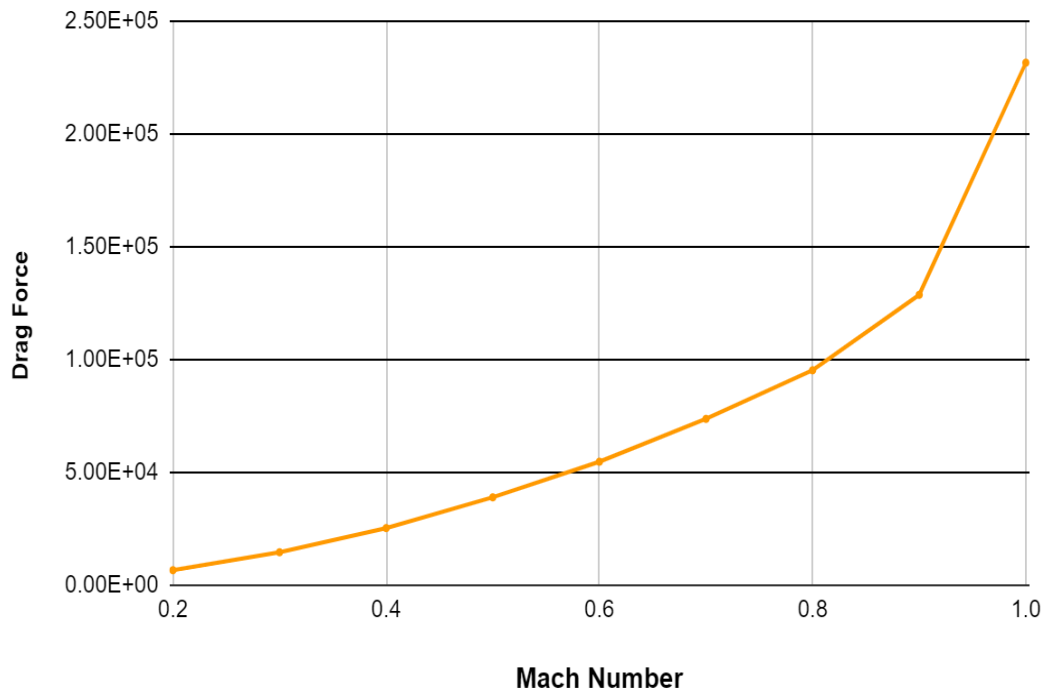


Fig 7.2: Drag force vs Mach number for Ellipse

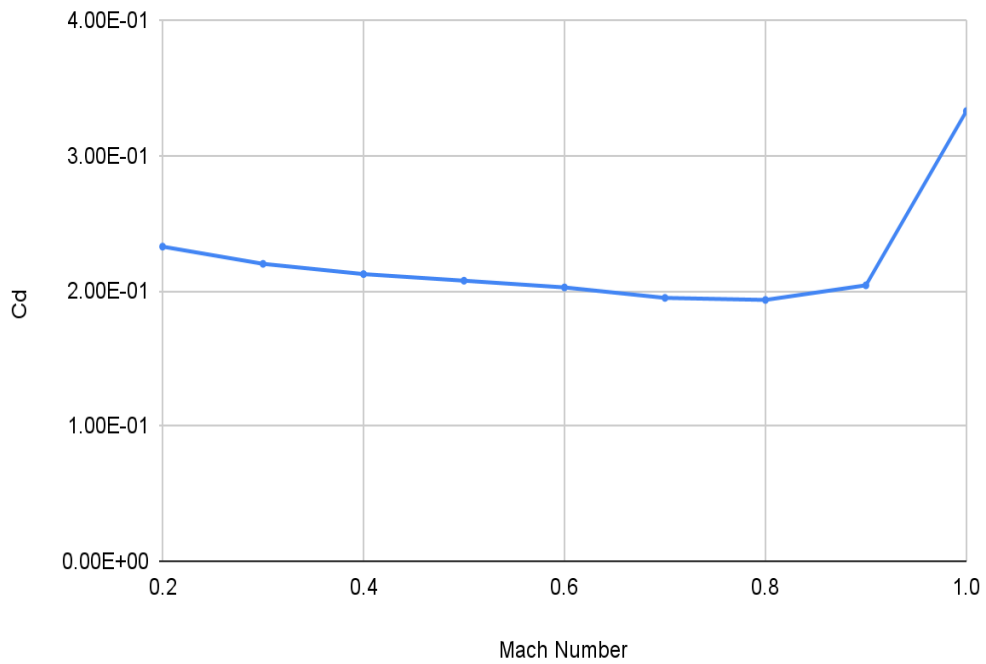


Fig 7.3: C_d vs Mach number for Power series

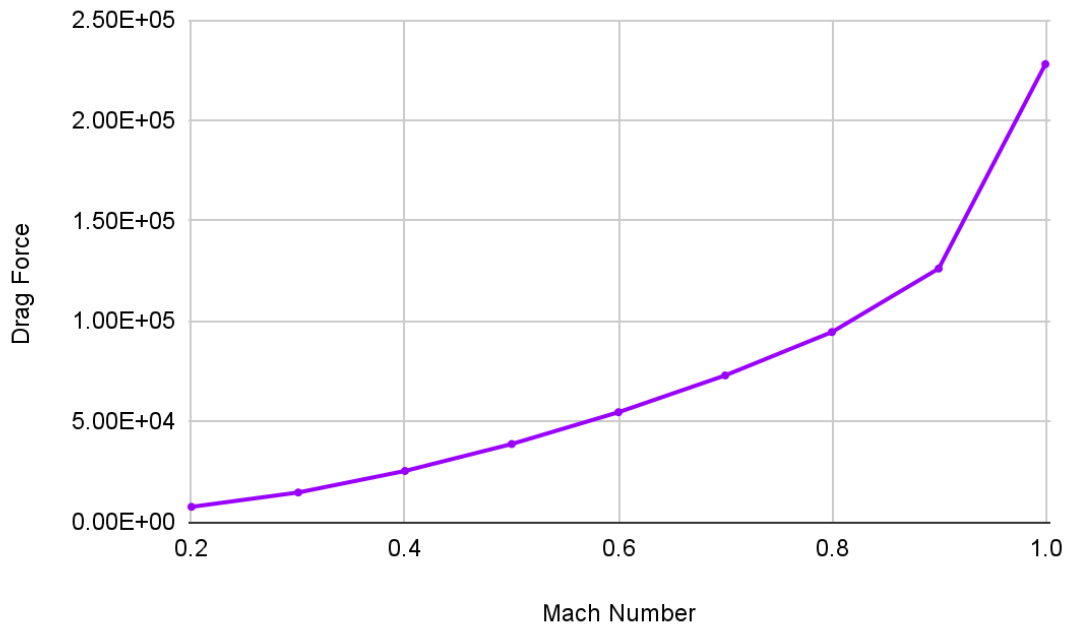


Fig 7.4: Drag Force vs Mach Number for Power Series

The morphing nose cone would have phase 1 (ellipse) undergo simulations at Mach 0.2 and Mach 0.3. Then phase 2 would be simulated at Mach 0.4, phase 3 at Mach 0.5, phase 4 at Mach 0.6, phase 5 at Mach 0.7, and finally phase 6 (½ power series) at Mach 0.8, Mach 0.9, and Mach 1.

The resultant C_d values were tabulated and studied. It was found that in the simulation for different mach ranges, starting at 0.2 and going up to 1 in the supersonic regime, there was a dramatic increase in the C_d beyond mach 0.8, and between 0.3 and 0.7, C_d had decreased on average in the subsonic range.

All three models, the static ellipse, the static power series, and the morphing cone were subjected to the same simulated conditions.

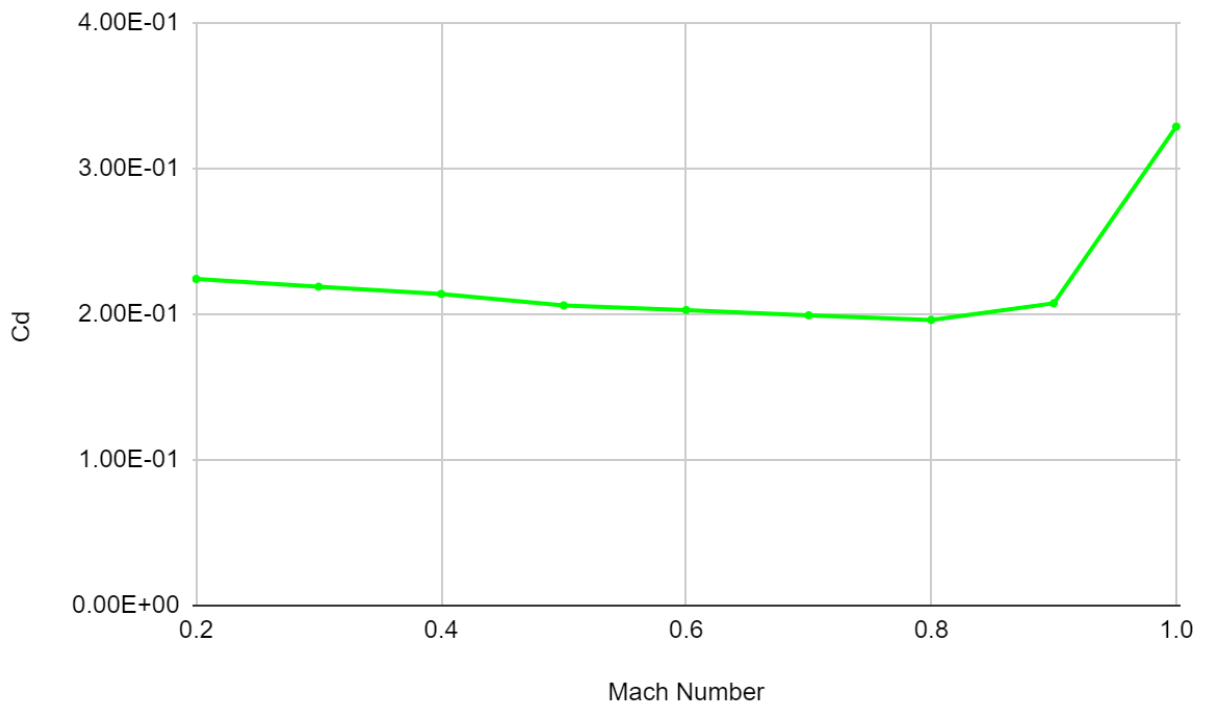


Fig 7.5: C_d vs Mach number for Morphed Cone

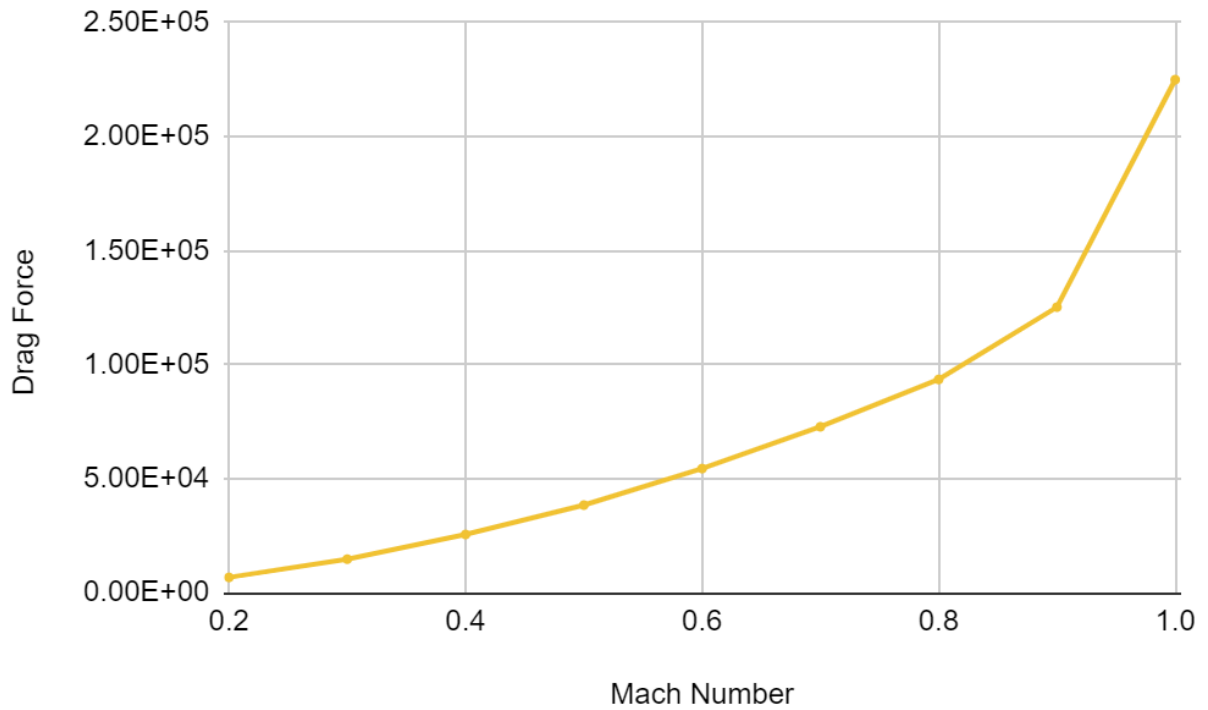


Fig 7.6: Drag Force vs Mach number for Morphed Cone

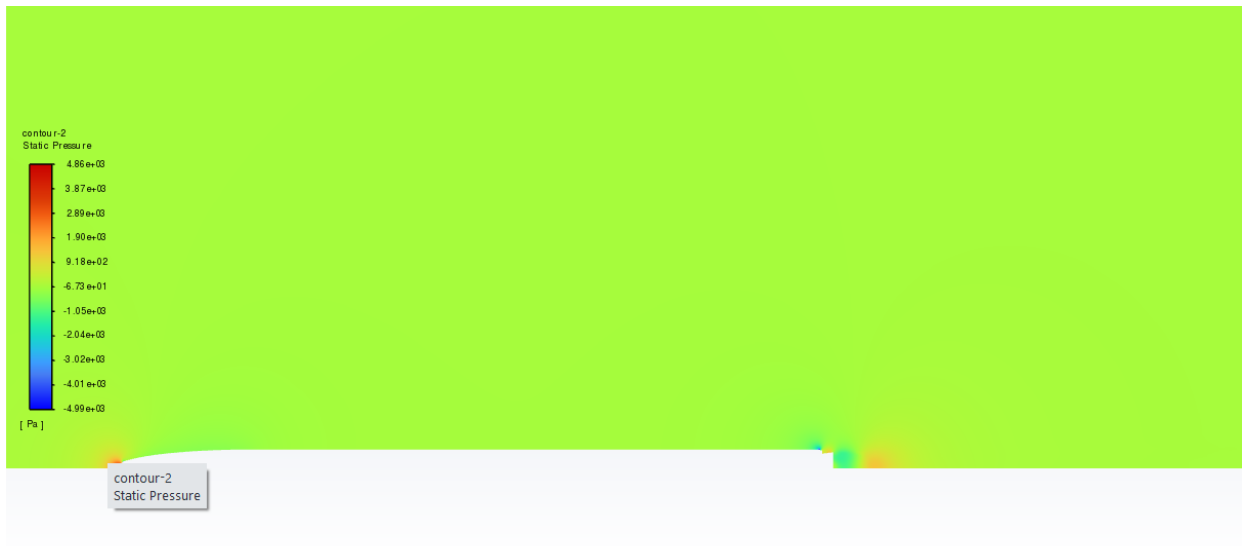


Fig 7.7: Pressure contours at Mach 0.3 for Phase 1



Fig 7.8: Velocity contours at Mach 0.3 for Phase 1

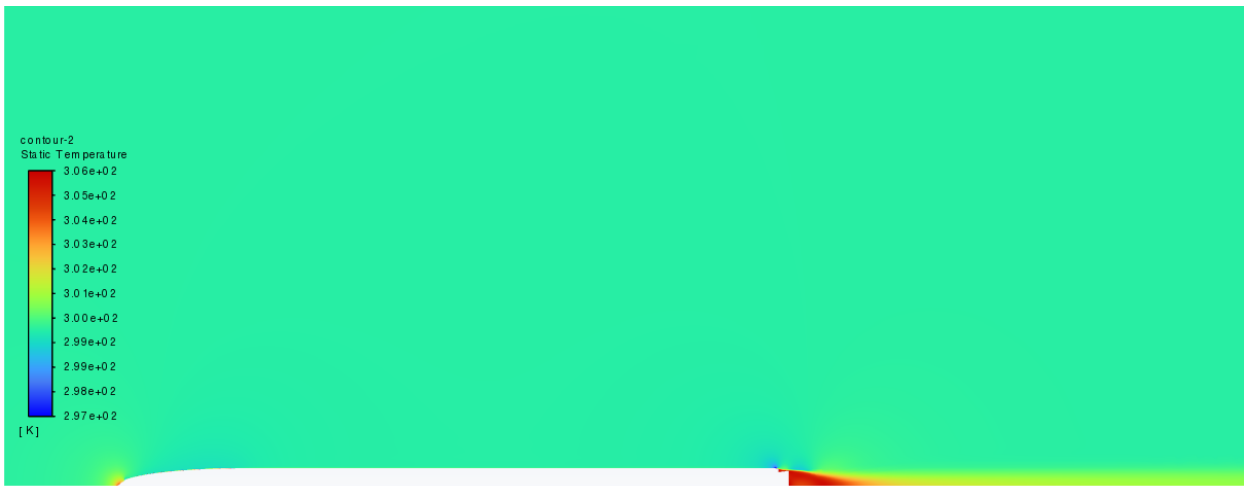


Fig 7.9: Temperature contours at Mach 0.3 for Phase 1



Fig 7.10: Velocity contour at Mach 0.4 for Phase 2



Fig 7.11: Temperature contour at Mach 0.4 for Phase 2

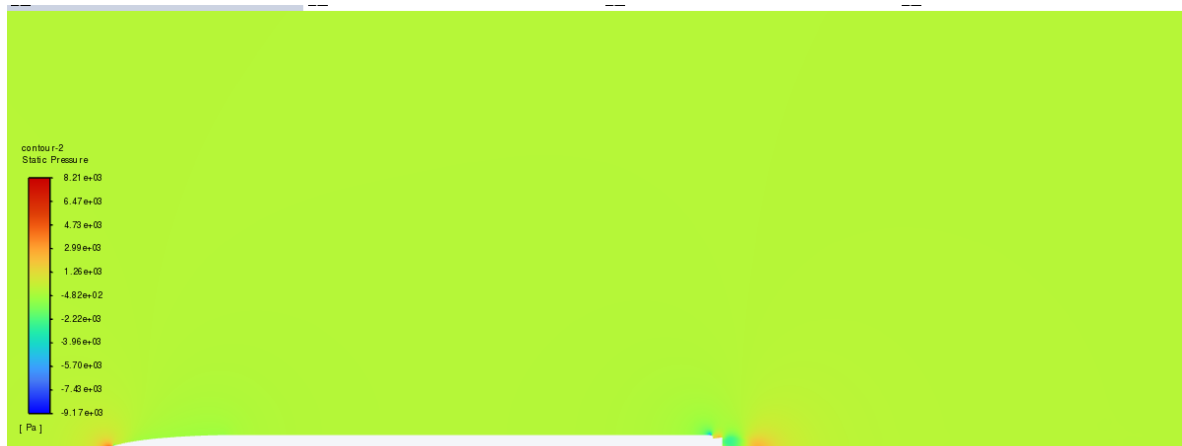


Fig 7.12: Pressure contour at Mach 0.4 for Phase 2



Fig 7.13: Velocity contour at Mach 0.5 for Phase 3



Fig 7.14: Pressure contour at Mach 0.5 for Phase 3

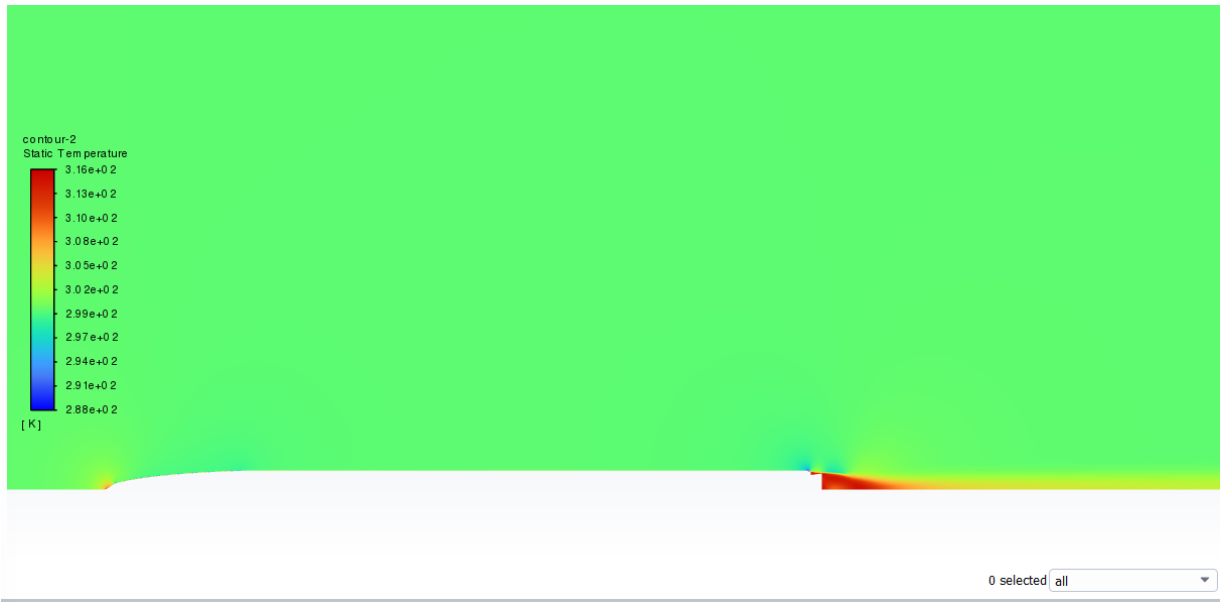


Fig 7.15: Temperature contour at Mach 0.5 for Phase 3



Fig 7.16: Velocity contour at Mach 0.6 for Phase 4

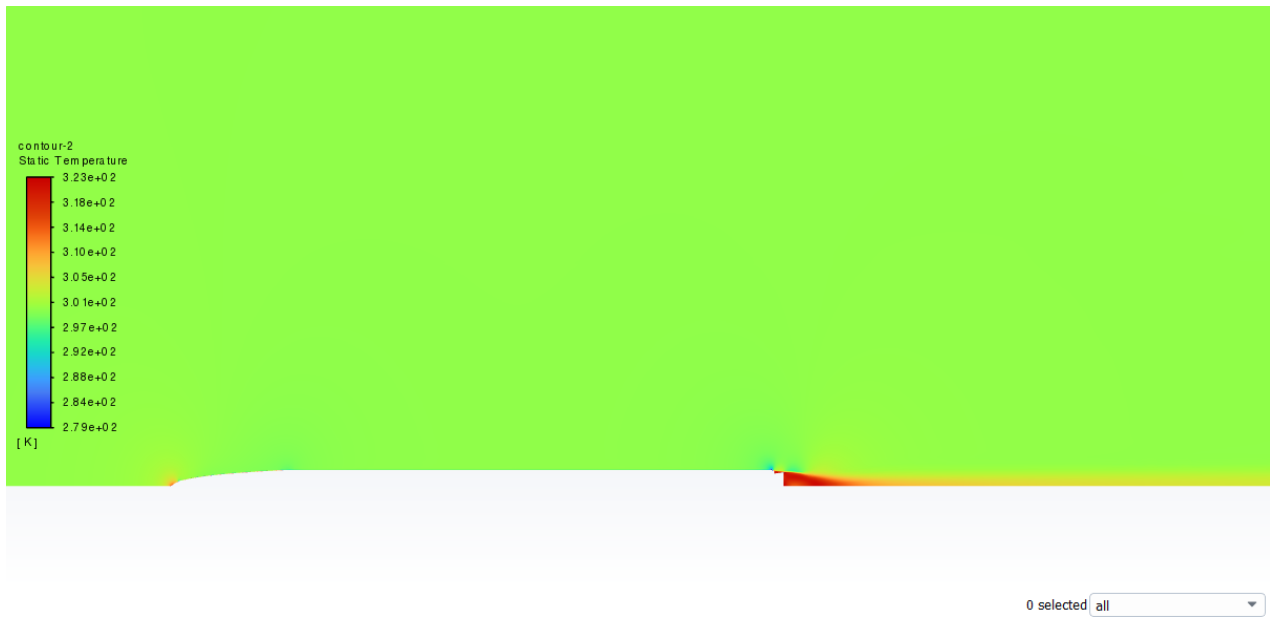


Fig 7.17: Temperature contour at Mach 0.6 for Phase 4



Fig 7.18: Pressure contour at Mach 0.6 for Phase 4



Fig 7.19: Velocity contour at Mach 0.7 for Phase 5



Fig 7.20: Pressure contour at Mach 0.7 for Phase 5



Fig 7.21: Temperature contour at Mach 0.7 for Phase 5



Fig 7.22: Temperature contour at Mach 0.8 for Phase 6



Fig 7.23: Velocity contour at Mach 0.8 for Phase 6



Fig 7.24: Pressure contour at Mach 0.8 for Phase 6

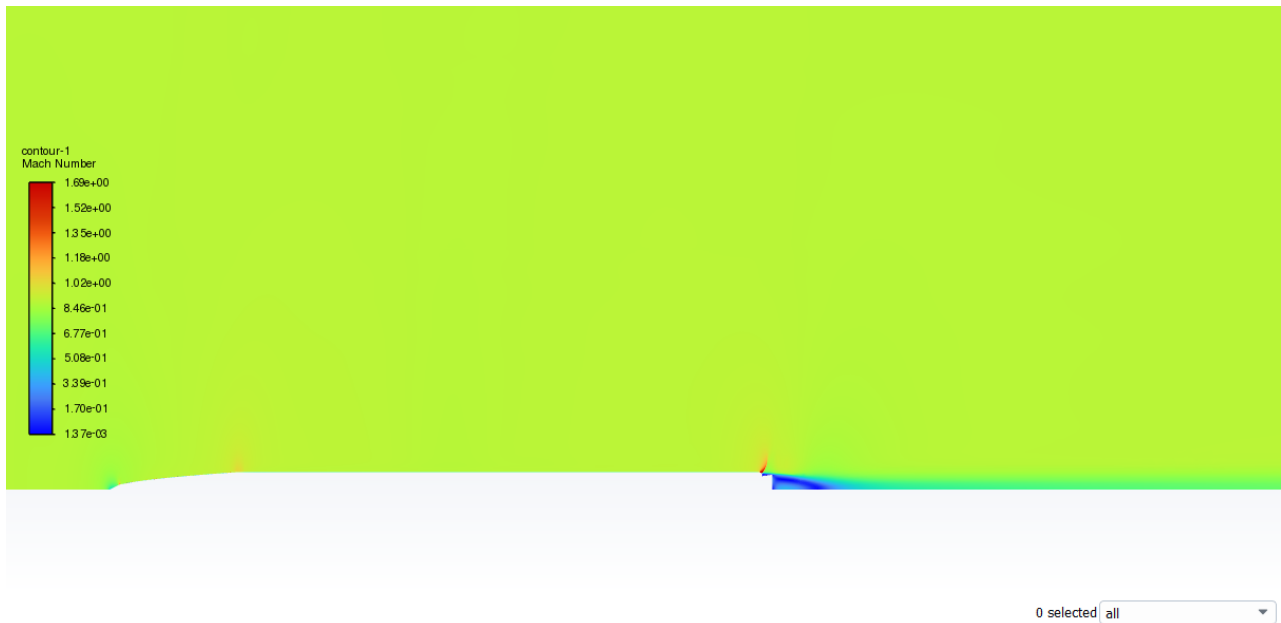


Fig 7.25: Velocity contour at Mach 0.9 for Phase 6



Fig 7.26: Temperature contour at Mach 0.9 for Phase 6



Fig 7.27: Pressure contour at Mach 0.9 for Phase 6

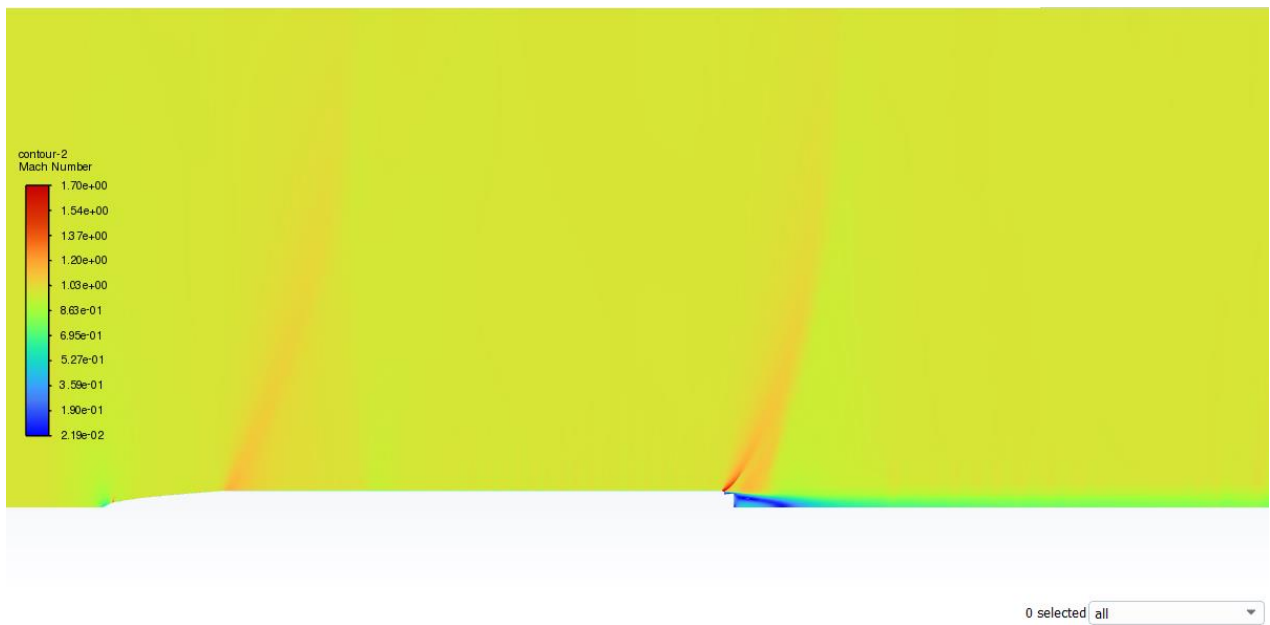


Fig 7.28: Velocity contour at Mach 1 for Phase 6

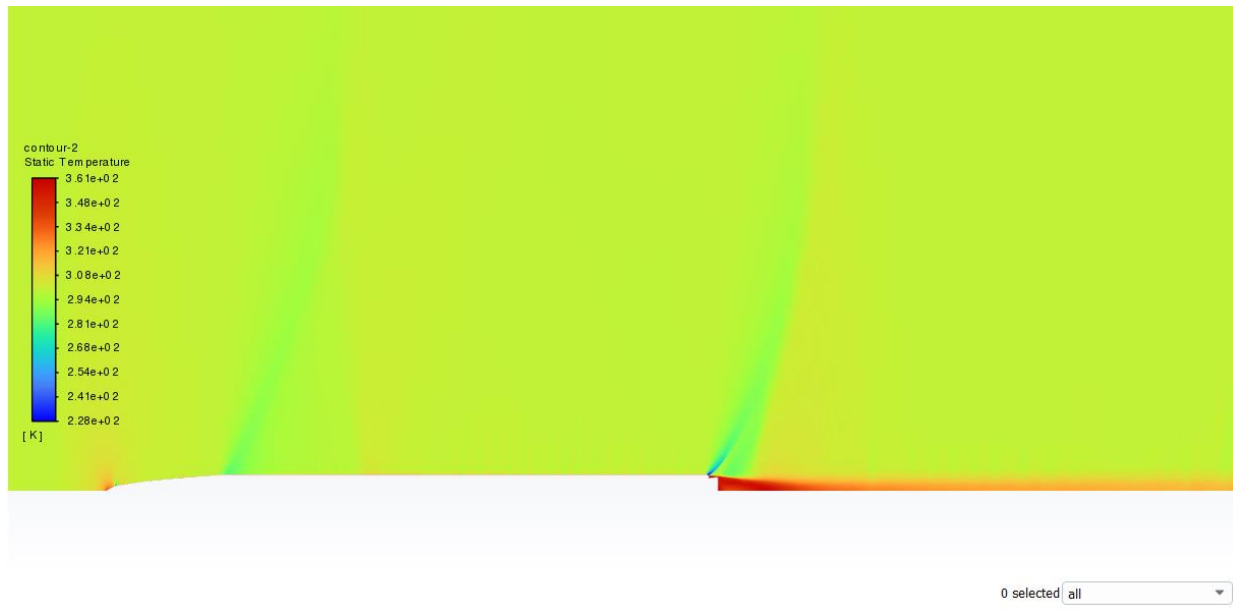


Fig 7.29: Temperature contour at Mach 1 for Phase 6

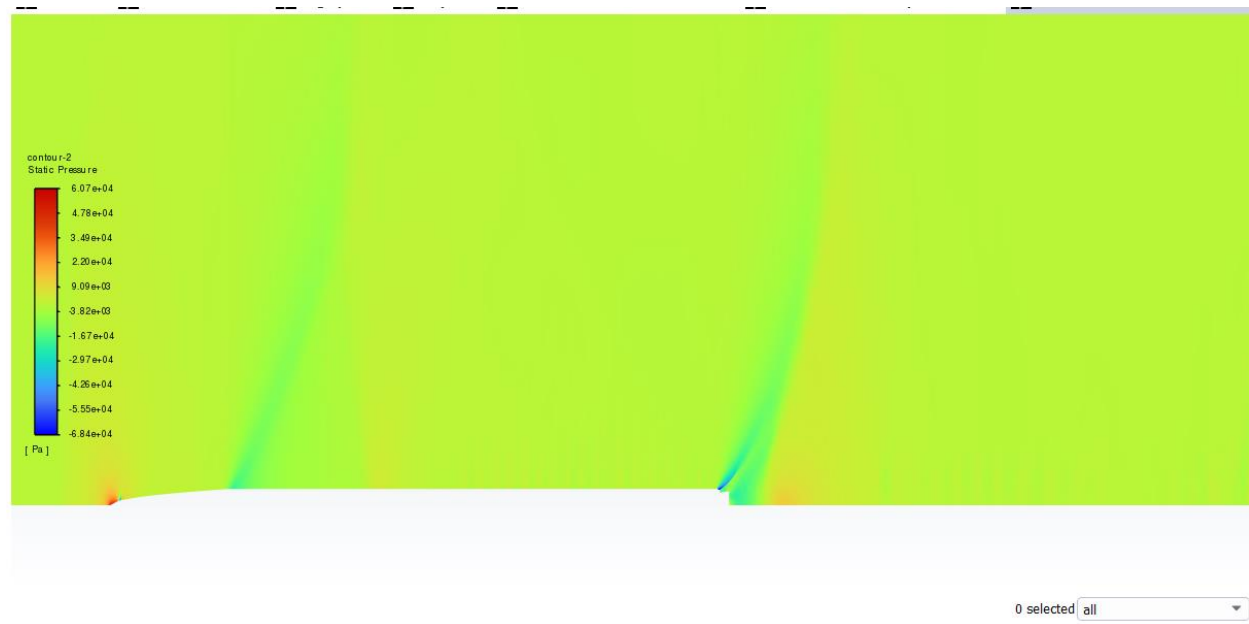


Fig 7.30: Pressure contour at Mach 1 for Phase 6

Upon comparing the data collected, it was shown that the elliptical cone had the least C_d between 0.2 to 0.4 beyond which it has a drastic increase. The morphed cone had better results than at least one of the two static cones at any point, and attained lower C_d (0.32891) than the static power series cone (0.33284) at Mach 1.

Table 7.1: C_d values for ellipse, power series and morphed nose cone for comparison

Mach Number	Coefficient of Drag(C_d)			Comparison of C_d	
	Morph	Ellipse	Power	Morph Vs Ellipse	Morph Vs Power
0.2	2.24E-01	2.21E-01	2.33E-01	0.0038 (1.53% increase)	0.0083 (3.58% decrease)
0.3	2.19E-01	2.18E-01	2.20E-01	0.00079 (0.36% increase)	0.00091 (0.41% decrease)
0.4	2.14E-01	2.13E-01	2.12E-01	0.00137 (0.64% increase)	0.0017 (0.8% increase)
0.5	2.06E-01	2.09E-01	2.07E-01	0.00318 (1.54% decrease)	0.0013 (0.62% decrease)
0.6	2.03E-01	2.04E-01	2.02E-01	0.00129 (0.63% decrease)	0.00047 (0.23% decrease)
0.7	1.99E-01	2.02E-01	1.95E-01	0.00277 (1.38% decrease)	0.00461 (2.63% increase)
0.8	1.96E-01	2.00E-01	1.93E-01	0.00375 (1.91% decrease)	0.00297 (1.53% increase)
0.9	2.08E-01	2.13E-01	2.04E-01	0.00584 (2.81% decrease)	0.00354 (1.73% increase)
1.0	3.29E-01	3.64E-01	3.33E-01	0.0347 (10.54% decrease)	0.00393 (1.19% decrease)

CD VS Mach No

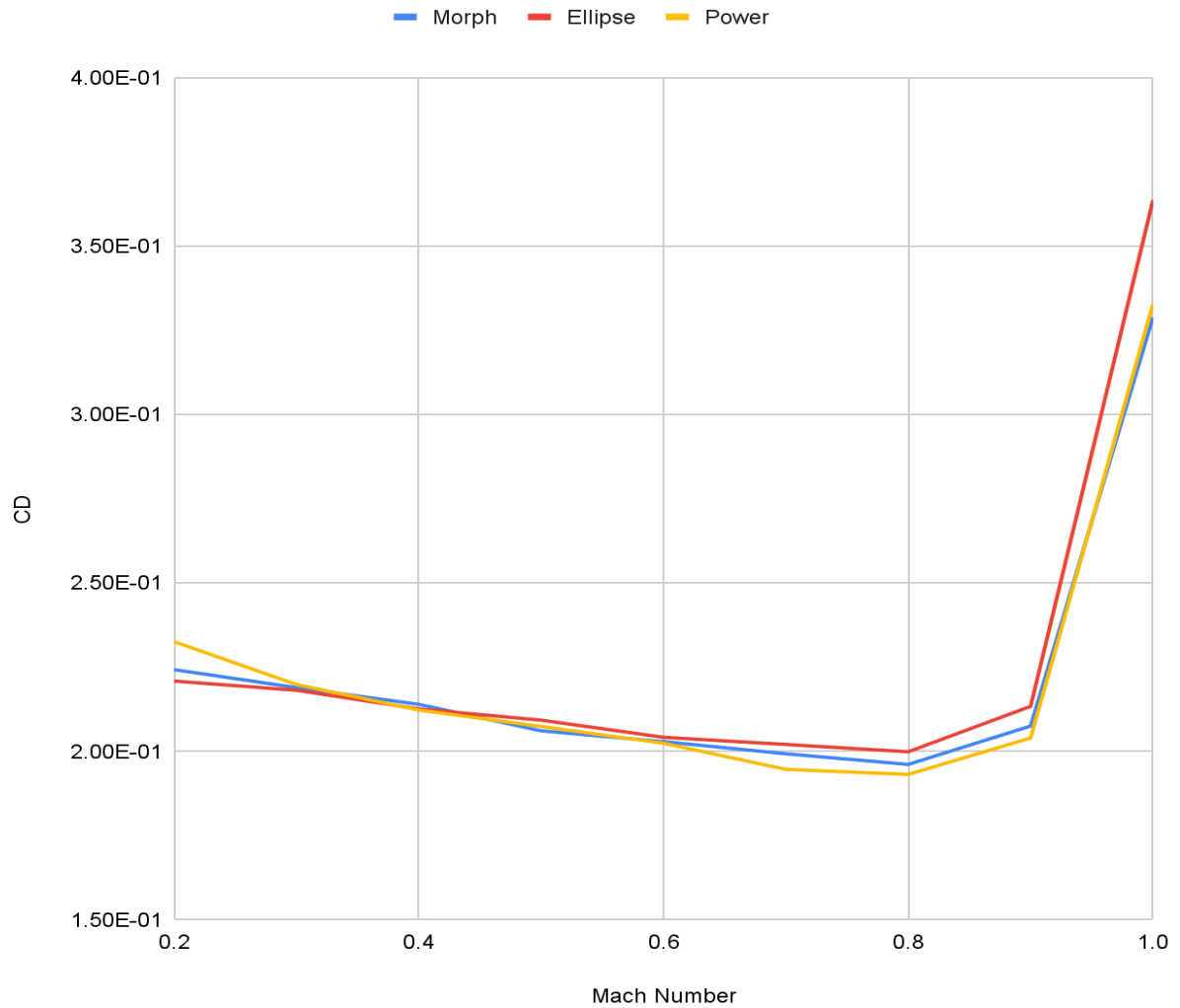


Fig 7.31: Comparison of C_d vs Mach Characteristics for Morphed Nose cone, Elliptical Nose cone, and $\frac{1}{2}$ Power series

8. FUTURE ENHANCEMENT AND CONCLUSION

Future works include the morphing of nose cones between 2 different shapes further in supersonic regime

With more time and computer resources available, the mesh may be fine-tuned to eliminate any numerical imperfections. Additional nose cone profiles, such as the $\frac{3}{4}$ parabola, Von Karman, and others, could be analysed in conjunction with the varied profiles to further investigate an optimised design in terms of geometry. Wind tunnel testing could be used to complete experimental testing of the nose cone profiles if possible.

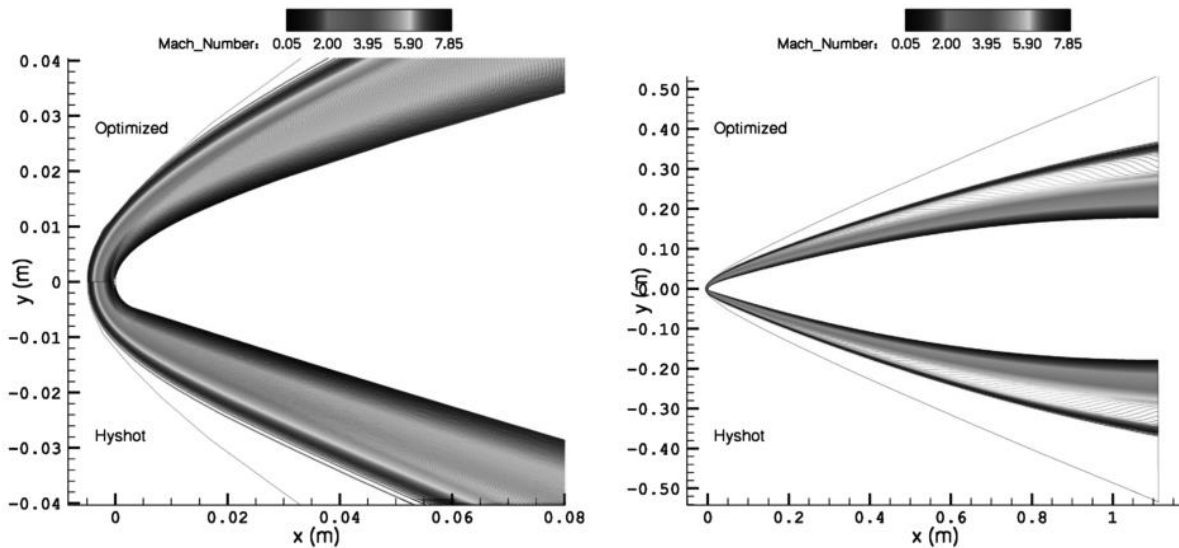


Fig 8.1: Example for Morphing Supersonic Nose Cone

For improved performance in subsonic and supersonic zones, a different variation in rib movement can be used. Individual rib movement can be adjusted according to the rocket's velocity, rather than being linearly varied as we did in our project. For various velocity regimes from subsonic to transonic to supersonic, it may provide a better outcome and a more optimised form for less drag.

The hypothetical model in this paper could be made out of active materials like SMA or other advanced materials that can alter shape in response to active controls. The mechanism could also be built using future technology, allowing the ribs to move further while maintaining the original arc length.

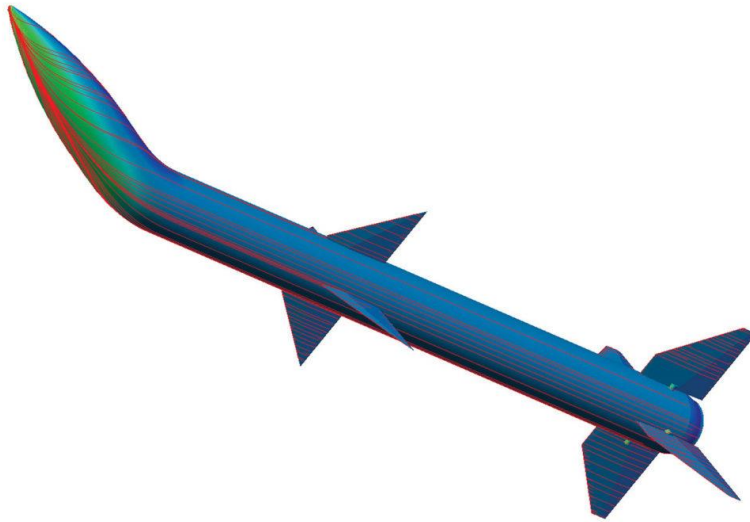


Fig 8.2: Change in Angle of Attack using Morph Nose cone

The angle of attack (AoA) can be adjusted, and the nose cone could also operate as an active control system, assisting in the rocket's or missile's guiding from its initial position to its target position. As a result, multiple active controls could well be eliminated, reducing the weight of the rocket while simultaneously increasing its manoeuvrability.

Though the potential is vast, the concept still has a long way to go because it requires a lot of experimental studies, ground testing, and numerous empirical results to make it fully practical for industry use.

8.1 Conclusion

In conclusion, nose cone geometry was designed based on the conditions of the rocket's flight path. The design was morphed and studied using phase transformations based on aerodynamic factors, and engineering design process for the given flight profile. This analysis was done utilizing ANSYS Fluent to conduct CFD on various 2D axisymmetric nose cone profiles of varying shapes. Based on the criteria of minimum drag, the morphed nose cone was optimal. The setup and the data itself were validated through a variety of methods. The C_d values of the comparison were well within the range, with the difference being attributed to the unknowns in setup conditions

The results obtained show that morphing the nose cone of a rocket could decrease the drag in subsonic and transonic regions. While not an immediately viable concept, it is nevertheless a promising direction to focus on when looking to improve drag efficiency, especially when newer, innovative methods are created that can improve the morphing mechanism of the nose cone.

9. REFERENCES

1. Stephen, Eric J., Thomas E. McLaughlin, Brett Bixler, Benjamin Dickinson, and Joshua Turner (2012). "Investigation of Nose Cone Enhancement to Improve the Effectiveness of an Articulating Nose Cone on a Subsonic Missile." In AIAA Aviation 2019 Forum , p. 3165
2. Iyer, Aditya Rajan; Pant, Anjali (August 2020). "A Review on Nose Cone Designs for Different Flight Regimes".International Research Journal of Engineering and Technology. 7 (8): 3546–3554.
3. J. Zhao, Y.L Zhang, W.H Chen, X. Guo, S.Z. Yan, G.T. Hu, Y. Yuan, P.F. Guo, Q.Y. Cai, 'Biomimetic Skeleton Structure of Morphing Nose Cone for Aerospace Vehicle Inspired by Variable Geometry Mechanism of Honeybee Abdomen', Aerospace Science and Technology (June 2019)
4. J.L. Li, J.N. Wu, S.Z. Yan, Conceptual design of deployment structure of morphing nose cone, Adv. Mech. Eng. 5 (2013) 59095
5. Wanhill, R.J., Ashok, B. "Shape Memory Alloys (SMAs) for Aerospace Applications" Aerospace Materials and Material Technologies. Chapter 21. Published in Singapore, 2017.
6. Gary A. Crowell Sr., "The Descriptive Geometry of Nose Cone," (1996)
7. Department of Defense. "Design of Aerodynamically Stabilized Free Rockets." Military Handbook. Published 17 July 1990.
8. Crowell, Gary Sr. "The Descriptive Geometry of Nose Cones". United States Patents. 11 Apr 1996.
http://www.if.sc.usp.br/~projetosufos/artigos/NoseCone_EQN2.PDF.
Accessed 21 Apr 2018.
9. Valasek J. Morphing Aerospace Vehicles and Structures (Aerospace Series), John Wiley & Sons, New York, USA, 2012
10. Stengel R F. Morphing aerospace vehicles and structures. Journal of Guidance, Control, and Dynamics, 2013, 36, 1562–1563

11. Otsuka, Wayman. "Shape Memory Materials" Cambridge University Press, Cambridge, 1999.
12. u J, Yan S, Gu Y. On stability optimization of the deployable bistable compliant structures mounted in the morphing skin: Method and implementation. Proceedings of the Institution of Mechanical Engineers, Part C: Journal of Mechanical Engineering Science, 2015, 229, 943–956
13. Galantai V P, Sofla A Y N, Meguid S A, Tan K T, Yeo W K. Bio-inspired wing morphing for unmanned aerial vehicles using intelligent materials. International Journal of Mechanics and Materials in Design, 2012.
14. Murugan S, Friswell M I. Morphing wing flexible skins with curvilinear fiber composites. Composite Structures, 2013, 99, 69–75.
15. Weisshaar T A. Morphing Aircraft Technology-New Shapes for Aircraft Design, Purdue University, Indiana, USA, 2006.
16. Hartl, Darren. Lagoudas, Dimitris. "Aerospace Applications of Shape Memory Alloys" Aerospace Engineering Department, Texas A&M University. 2017.
17. Mardanpour P, Hodges D H. Passive morphing of flying wing aircraft: Z-shaped configuration. Journal of Fluids and Structures, 2014.